Floquet analysis of frequency collisions

Kentaro Heya,[1,*] Moein Malekakhlagh,[1] Seth Merkel,[1] Naoki Kanazawa,[2] and Emily Pritchett[1]

[1]*IBM Quantum, IBM T.J. Watson Research Center, Yorktown Heights, New York 10598, USA*

[2]*IBM Quantum, IBM Research Tokyo, 19-21 Nihonbashi Hakozaki-cho, Chuo-ku, Tokyo 103-8510, Japan*

Implementation of high-fidelity gate operations on integrated-qubit systems is vital for fault-tolerant quantum computation. Qubit-frequency allocation is an essential part of improving control fidelity. A metric for qubit-frequency allocation, frequency collision, has been proposed on simple systems of only a few qubits driven by a monomodal microwave drive. However, frequency allocation for quantum processors for more advanced purposes, such as quantum error correction, needs further investigation. In this study, we propose a Floquet analysis of frequency collisions. The key to our proposed method is a reinterpretation of frequency collisions as an unintended degeneracy of Floquet states, which allows a collision analysis on more complex systems with many qubits driven by multimodal microwave drives. Although the Floquet state is defined in an infinite-dimensional Hilbert space, we develop algorithms, based on operation perturbation theory, to truncate the Hilbert space down to the optimal computational complexity. In particular, we show that the computational complexity of the collision analysis for a sparse qubit lattice is linear with the number of qubits. Finally, we demonstrate our proposed method on cross-resonance-based experimental protocols. We first study the cross-resonance gate in an isolated three-qubit system, where the effectiveness of our method is verified by comparing it with previous studies. We next consider the more complex problem of syndrome extraction in the heavy-hexagon code [Christopher et al., Phys. Rev. X **10**, 011022 (2020). doi:10.1103/PhysRevX.10.011022]. Our proposed method advances our understanding of quantum control for quantum processors and contributes to their improved design and control.

DOI: 10.1103/PhysRevApplied.21.024035

I. INTRODUCTION

There has been remarkable progress in quantum computer engineering toward the realization of large-scale fault-tolerant quantum computation [1]. In particular, superconducting circuits are among the most promising quantum platforms due to their compatibility with conventional transistor fabrication processes, microwave control technology in communication wavelength bands [2–4], and progress towards long-range three-dimensional (3D) integration [5–7]. Superconducting quantum processors with several hundred qubits [8] allow demonstrations of quantum error correction [9–11], [11–17]. However, the number of physical qubits required for fault-tolerant quantum computing is strongly dependent on physical gate fidelity. It is therefore imperative to further improve physical gate fidelity.

Superconducting circuits can be broadly classified into those with and without a tunable Josephson junction [18]. Tunable-circuit architectures allow dynamic control of circuit parameters and are generally superior in terms of the execution time of entangling gates and system flexibility, but they suffer from sensitivity to external flux noise [19–25]. The fixed-circuit architectures, on the other hand, use fixed-circuit parameters, resulting in a relatively simple implementation with excellent scalability, stability, and coherence [26–35]. However, fixed-circuit architectures lack flexibility as their performance is highly dependent on designed circuit parameter values. Qubit-frequency allocation is therefore highly significant, especially for fixed-frequency architectures.

Frequency collisions [36–40] were introduced as a guideline for designing circuits that use the cross-resonance (CR) gate [41–43], a widely used microwave-activated entangling gate amenable to fixed-frequency architectures. Frequency collisions can be estimated numerically by time-domain simulation of the full CR Hamiltonian [39] or analytically using time-independent or time-dependent Schrieffer-Wolff perturbation under the rotating-wave approximation (RWA) of the drive Hamiltonian [43–46]. Reference [36] characterizes frequency collisions for the standard CR gate with consideration of a spectator qubit by looking into the poles of the effective Hamiltonian while sweeping system parameters. Effective

*Kentaro.Heya1@ibm.com

and adequate for isolated systems, numerical approaches are impractical for larger systems, and time-independent perturbation under RWA is only valid for the time-periodic monomodal Hamiltonian. In general, for a multimodal Hamiltonian, there is no obvious choice of a rotating frame that makes the Hamiltonian time independent [47]. Therefore, the standard methods are not applicable, for example, to simultaneous CR gates [17], other multimodal gates, such as cross-cross resonance gate [29], or systems where interactions with detuned spectator qubits are relevant [47]. In Ref. [38], on the other hand, an analysis of frequency collisions in flux-activated entangling gates [21] reveals that collisions are caused by accidental degeneracies of energy levels during flux-bias sweeps, both in isolation and in parallel with simultaneous flux-bias sweeps. Note, however, this analysis applies only when the Hamiltonian is approximately time independent during the gate.

In this paper, we redefine frequency collision by means of a more general and unified framework based on Floquet theory [48]. Floquet theory introduces frequency-domain analysis to frequency collisions, which are commonly analyzed in the time domain [39,49]. It characterizes frequency collisions as the breakdown of strong-dispersive condition of the Floquet Hamiltonian expressed in the desired operation basis. To distinguish such frequency-domain frequency collisions from the previous notions, we call them "Floquet collisions." The degree of Floquet collision is quantified as a collision angle between Floquet states, and the degree of fidelity deterioration caused by Floquet collisions can also be estimated from the collision angle and the effective coupling strength between the colliding Floquet states. Because the Floquet Hamiltonian is infinite dimensional, we propose a perturbative approach [50] to derive the collision angles with a finite computational cost. We also discuss a relationship between Floquet collision and qubit lattice structure in real space, and propose an efficient collision analysis method for the sparse qubit lattice that requires only a linear computational cost with respect to the number of qubits.

We demonstrate our Floquet-based collision analysis on analytical and numerical simulations. First, for CR gates on an isolated-transmon system, we provide analytical solutions of Floquet collisions in terms of collision angles between Floquet states and re-examine the frequency collisions in Ref. [46]. Our Floquet-based collision analysis can be applied to an arbitrary parameter region, and allows for the calculation of the intensity and bounds of collisions, which extends the discussion in Refs. [39,49]. Second, we calculate and visualize the collision angles numerically while sweeping various system parameters such as qubit frequencies, CR drive amplitude, and rotary tone drive amplitude [42,51]. Our numerical simulations reveal collisions originating from microwave drive, which have not been reported before. These findings will

contribute to the optimal pulse shaping of the CR gate in the future. Third, we consider a more complex system of an error-correction code. Here, we focus on syndrome extraction in heavy-hexagon codes [17,52], quantitatively estimating the difficulty of system-frequency allocation. Our measures provide an approximate estimate of the computational cost to improve the system-frequency allocation for large-scale error correction in the future.

The rest of the main text is organized as follows: In Sec. II, we review Floquet theory, and our reinterpretation of frequency collisions. In Sec. III, we review generalized perturbation theory and apply it to find Floquet collisions. We also discuss the relationship between Floquet collision and distance in Floquet and real space. In Sec. IV, we summarize our Floquet-based collision analysis, and estimate the computational complexity of collision analysis. In Sec. V, we demonstrate our Floquet-based collision analysis by applying it to actual experimental conditions. Lastly, in Sec. VI, we summarize our results and provide directions for future work.

II. FREQUENCY COLLISION AND FLOQUET THEORY

Floquet theory [48] applies to linear differential equations with time-periodic generators, having a wide range of applications such as stability analysis [53,54], chemistry [55], and material physics [56,57]. In the context of quantum mechanics, a time-periodic Hamiltonian with continuous-wave (CW) drive is a prime example of a time-periodic generator [58,59]. We can also find recent applications to quantum information science such as analyzing time crystals [60], gate calibration [61], controlling driven qubits [33,34,62], protecting qubits from noise [63–65], improving a quantum parametric amplifier [66], and designing the adiabatic microwave-activated entangling gates [67].

In this section, we apply Floquet theory to the analysis of frequency collisions. Using Floquet theory, we can transform a finite-dimensional periodic time-dependent Hamiltonian into an infinite-dimensional time-independent Floquet Hamiltonian, instead of the common practice of transforming into a rotating frame under the RWA. Floquet theory enables analyzing frequency collisions in a multimodal Hamiltonian [29,33,62–65,68] and provides deeper insights into frequency collisions.

A. Floquet theory

Let us assume a *d*-dimensional system Hamiltonian $H(t)$. The Schrödinger equation in natural units is given as

$$\left(H(t) - i\frac{\mathrm{d}}{\mathrm{d}t}\right)\Phi(t) = 0, \tag{1}$$

where $\Phi(t)$ represents the fundamental solution matrix. According to Floquet theory, the fundamental solution matrix of a differential equation reads

$$\Phi(t) = e^{-iEt}\Psi(t), \tag{2}$$

where $\Psi(t)$ is a d-dimensional square matrix and E is a d-dimensional diagonal matrix. $\Psi(t)$ has the same time periodicity as $H(t)$ and can be decomposed by the discrete Fourier series expansion as

$$H(t) = \sum_{\vec{\mathbf{n}} \in \mathbb{Z}^{\|\vec{\omega}\|_0}} H^{(\vec{\mathbf{n}})} e^{i\vec{\mathbf{n}}\cdot\vec{\omega}t}, \tag{3}$$

$$\Psi(t) = \sum_{\vec{\mathbf{n}} \in \mathbb{Z}^{\|\vec{\omega}\|_0}} \Psi^{(\vec{\mathbf{n}})} e^{i\vec{\mathbf{n}}\cdot\vec{\omega}t}, \tag{4}$$

where $A^{(\vec{\mathbf{n}})}$ represents the $\vec{\mathbf{n}}$th coefficient of the discrete Fourier series expansion of the matrix A, and $\|\vec{\mathbf{x}}\|_p$ represents the L^p norm of the vector $\vec{\mathbf{x}}$. Then, we obtain the following eigenequation from the Schrödinger equation:

$$E_{ii}\Psi_{ij}^{(\vec{\mathbf{n}})} = \sum_{k,\vec{\mathbf{m}}} \left\{ H_{ik}^{(\vec{\mathbf{n}}-\vec{\mathbf{m}})} + (\vec{\mathbf{n}}\cdot\vec{\omega})\delta_{ik}\delta_{\vec{\mathbf{n}}\vec{\mathbf{m}}} \right\} \Psi_{kj}^{(\vec{\mathbf{m}})}, \tag{5}$$

where A_{ij} represents the (i,j) elements of the matrix A. Note that Eq. (5) is invariant except for a constant offset for any translation operation $\vec{\mathbf{r}}$ on the vector $\vec{\mathbf{n}}$.

Equation (5) can be interpreted as a time-independent energy-level diagram in infinite dimensions. In the following, we refer to this extended energy level diagram as the Floquet Hamiltonian and the subspace associated with index $\vec{\mathbf{n}}$ as the Brillouin zone BZ $(\vec{\mathbf{n}})$ [69]. The state $|\psi\rangle$ in BZ $(\vec{\mathbf{n}})$ is denoted as $|\psi;\vec{\mathbf{n}}\rangle$. We refer to the eigenvalues and eigenvectors of the Floquet Hamiltonian as Floquet quasiexcitation energies and Floquet states, respectively. The system time evolution $U(t';t)$ can be reconstructed as

$$U(t';t) = \Phi(t')\Phi(t)^\dagger \tag{6}$$

$$= e^{-iEt'}\Psi(t')\Psi^\dagger(t)e^{iEt}. \tag{7}$$

B. Frequency collision

In the context of quantum gates, a frequency collision refers to proximity to unwanted resonances that are detrimental to gate performance. The frequency collision can be static or dynamic, depending on the nature of the underlying transition and the role of drive photons. In a perturbative analysis, the position of frequency collisions can be identified as poles, while the collision width and nature is determined by the makeup of transition matrix elements in the numerator [36–40,49]. Using Floquet theory, collisions can be formulated more rigorously as a breakdown of the strong-dispersive condition [70,71] in the Floquet Hamiltonian. Figure 1 shows the general concept of our proposal. In this section, we calculate a fidelity between ideal propagators and those in the presence of a collision. This gives us a metric to numerically evaluate the impact of collisions on gate performance.
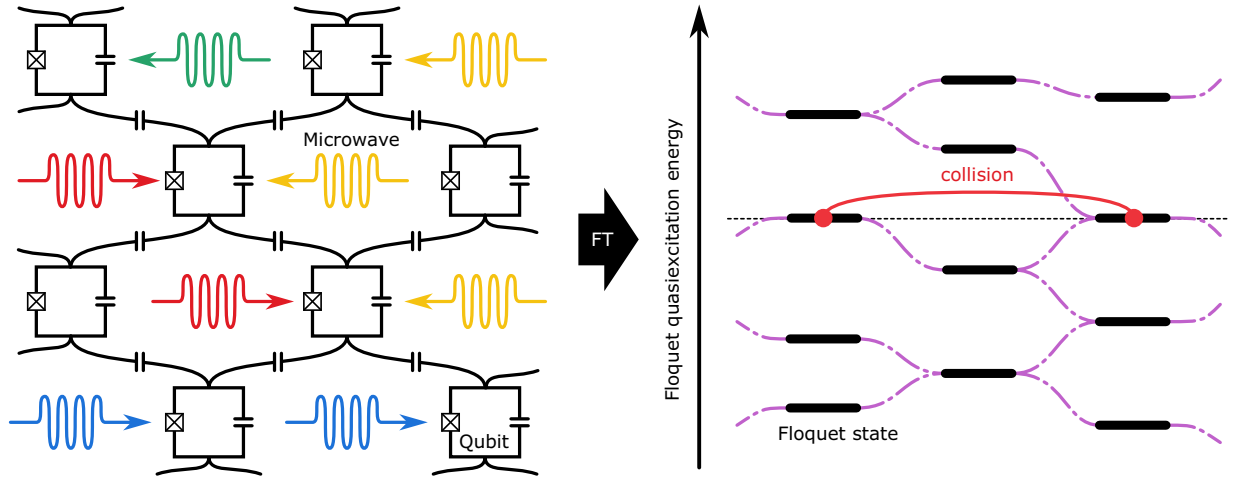

FIG. 1. Concept of our Floquet-based collision analysis. The left figure shows a general quantum control schematic. The qubits align in a planar lattice, and multiple microwaves are simultaneously irradiated. Some of the microwaves can be resonant with each other. Using Floquet theory and applying the Fourier transform (FT) to the Schrödinger equation corresponding to the left figure, we obtain a Floquet Hamiltonian and a corresponding energy-level diagram shown on the right. The black bold and purple dotted lines represent Floquet states and their couplings, respectively. If the Floquet Hamiltonian satisfies the strongly dispersive condition in the operation basis described in Sec. II B, we can control our system sufficiently. On the other hand, if Floquet states are degenerate, as shown in the right figure, Floquet collision occurs and the control fidelity deteriorates significantly.

To describe a given quantum gate, we pick a suitable Floquet basis $\{\psi_i\}$, which we generally refer to as the operation basis. In the context of the CR gate, this is often called the block-diagonal basis. To illustrate our method, consider the simple case of a Floquet subspace Hamiltonian spanned by two Floquet states $|\psi_A; n + m\rangle$, $|\psi_B; n\rangle$ in the operation basis with a drive frequency ω_d as follows:

$$H_{AB} = \Delta_{AB}\frac{Z_{AB}}{2} + 2g_{AB}\frac{X_{AB}}{2}, \tag{8}$$

where Δ_{AB} and g_{AB} represent the energy detuning and coupling strength between the Floquet states, and X_{AB} and Z_{AB} represents the Pauli X and Z operator defined on the subspace. The first and second terms represent the diagonal and nondiagonal elements of the Floquet Hamiltonian in the operation basis, respectively. Figure 2 shows the schematic of the energy level diagram corresponding to the Floquet subspace Hamiltonian.
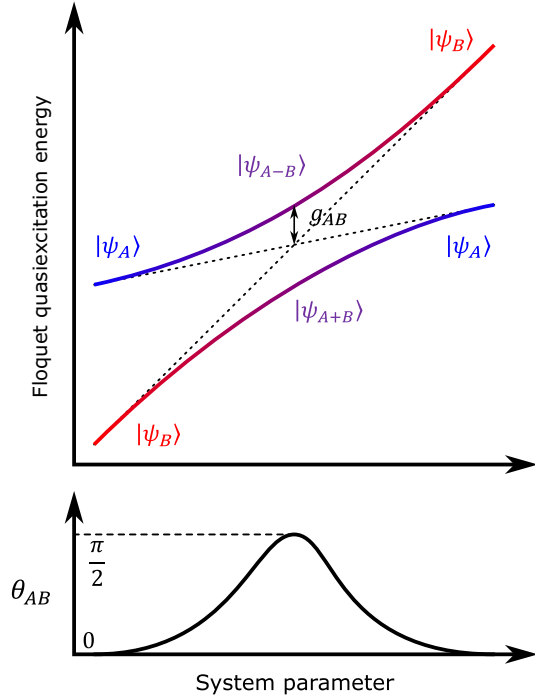

FIG. 2. (Top) A schematic for anticrossing between Floquet states $|\psi_{A,B}\rangle$. The top figure shows how Floquet quasiexcitation energy changes while sweeping a system parameter. We can find that an anticrossing occurs near a degenerate point of two Floquet states, where Floquet the quasiexcitation energy acquires an energy gap proportional to an effective coupling strength between the Floquet states. (Bottom) Dependence of collision angle θ_{AB} between the Floquet states $|\psi_{A,B}\rangle$ while sweeping system parameter. The collision angle becomes $\pi/2$ at the degenerate point and close to 0 under a strong-dispersive condition.

The matrix can be exactly diagonalized by the following rotational matrix:

$$R_Y(\theta) \equiv \exp\left(-i\theta\frac{Y_{AB}}{2}\right), \tag{9}$$

$$\theta = \arctan\left(\left|\frac{2g_{AB}}{\Delta_{AB}}\right|\right), \tag{10}$$

where Y_{AB} and θ represent the Pauli Y operator and the collision angle between the Floquet states, respectively. Thus, the diagonalized Floquet subspace Hamiltonian E_{AB} is found as

$$E_{AB} = R_Y(\theta)H_F R_Y(-\theta) = r\frac{Z_{AB}}{2}, \tag{11}$$

where $r = \sqrt{\Delta_{AB}^2 + 4g_{AB}^2}$ represents the energy detuning between the Floquet states. From Eq. (4), the periodic functions on the subspace spanned by the Floquet states are reconstructed as

$$\Psi(t) = R_Y(\theta)R_Z(m\omega_d t)\begin{pmatrix} |\psi_A\rangle \\ |\psi_B\rangle \end{pmatrix}, \tag{12}$$

where a global phase is omitted for simplicity. Then, from Eqs. (2) and (7), the propagator from time 0 to T is found as

$$U_{AB}(T; 0) = R_Z(rT)\Psi(T)\Psi^\dagger(0) \tag{13}$$

$$= R_Z(rT)R_Y(\theta)R_Z(m\omega_d T)R_Y(-\theta). \tag{14}$$

Without impact from a collision, we would expect $U_{AB}(T; 0) = R_Z(\Delta_{AB}T)R_Z(m\omega_d T)$, so from Eq. (14), Floquet collisions cause two types of gate errors simultaneously: axial rotation $R_Y(\theta)$ and phase shift $R_Z((r - \Delta_{AB})T)$.

In the ideal case, Floquet Hamiltonian satisfies the strong-dispersive condition $g_{AB} \ll \Delta_{AB}$ or $\theta_{AB} \sim 0$ in the operation basis. The ideal subspace propagator $V_{AB}(T; 0)$ designed under the strong-dispersive condition is obtained by linearly approximating the real subspace propagator $U_{AB}(T; 0)$ as

$$V_{AB}(T; 0) = R_Z(v_0)\begin{pmatrix} v_1 & v_3 \\ v_3 & v_2 \end{pmatrix}, \tag{15}$$

where v_i read

$$v_0 = \Delta_{AB} T \left\{ 1 + \frac{1}{2} \left(\frac{2g_{AB}}{\Delta_{AB}} \right)^2 \right\}, \tag{16}$$

$$v_1 = 1 + e^{im\omega_d T} \left(\frac{2g_{AB}}{\Delta_{AB}} \right)^2, \tag{17}$$

$$v_2 = e^{im\omega_d T} + \left(\frac{2g_{AB}}{\Delta_{AB}} \right)^2, \tag{18}$$

$$v_3 = \left(1 - e^{im\omega_d T} \right) \left(\frac{2g_{AB}}{\Delta_{AB}} \right). \tag{19}$$

Thus, the inner product of the gates in the subspace is written as follows:

$$f_{AB} = \frac{1}{2} \mathrm{Tr} \left[U_{AB}(0;T) V_{AB}^\dagger(0;T) \right] \tag{20}$$

$$\geq \frac{1}{2} \mathrm{Tr} \left[U_{AB}(0;T) R_Z \left(-(\Delta_{AB} + m\omega_d)T \right) \right] \tag{21}$$

$$= \cos^2 \left(\frac{\theta}{2} \right) \cos \left(\frac{\delta r T}{2} \right) + \sin^2 \left(\frac{\theta}{2} \right)$$

$$\times \cos \left(\left(\frac{\delta r}{2} + m\omega_d \right) T \right), \tag{22}$$

where $\delta r = r - \Delta_{AB}$.

Let us assume a D-dimensional Hilbert space, where we have no Floquet collision except for the two Floquet states $|\psi_{A,B}\rangle$. Then, the Floquet Hamiltonian of the whole space is expressed as follows:

$$\mathcal{H} = \left(\begin{array}{c|c} H_\perp & H_{\mathrm{int}} \\ \hline H_{\mathrm{int}} & H_{AB} \end{array} \right), \tag{23}$$

where $H_\perp$ and H_{int} represent the Floquet Hamiltonian in the outside of the subspace and the interaction term between the inside and the outside of the subspace, respectively. From Eq. (11), we can diagonalize the Floquet subspace Hamiltonian H_{AB} as

$$E = (I_\perp \otimes R_Y(\theta)) H (I_\perp \otimes R_Y(-\theta)), \tag{24}$$

$$= \left(\begin{array}{c|c} H_\perp & H_{\mathrm{int}} R_Y(-\theta) \\ \hline R_Y(\theta) H_{\mathrm{int}} & E_{AB} \end{array} \right), \tag{25}$$

where $I_\perp$ represent the identity operator in the outside of the subspace. Because the subspace-diagonalized Floquet Hamiltonian E satisfies the strong-dispersive condition, we can solve the time evolution driven by E perturbatively. Thus, the inner product of the gates in the whole space is

approximated as follows:

$$f = \frac{D-2}{D} + \frac{2}{D} f_{AB} + \mathcal{O}(g_{\mathrm{AB}} H_{\mathrm{int}}^2). \tag{26}$$

Consequently, the entangling fidelity [72] derived from the Floquet collision is calculated as follows:

$$\mathcal{F}(U, V) \equiv |f|^2. \tag{27}$$

In the above, we dealt with the case where two Floquet states are degenerate with each other. However, in realistic cases as described in Sec. V B, it is possible for multiple Floquet states to collide simultaneously under certain system parameters. In such a situation, we can follow the same procedure by diagonalizing the subspace spanned by the colliding Floquet states. We also have a simpler approach to account for individual Floquet collisions independently, and estimate approximate lower bounds of the gate fidelity. From a derivative of Gershgorin circle theorem [73], we can bound the shift of the Floquet quasiexcitation energy detuning δr_{ij}, and the collision angles $\delta\theta_{ij}$ between ith and jth Floquet states, defined on the Floquet subspace $\mathcal{S}$ spanned by simultaneously colliding Floquet states, as follows:

$$|\delta r_{ij}| \leq \delta r_{ij}^{\mathrm{max}} = \sum_{k \in \mathcal{S}} \left(|g_{ik}| + |g_{jk}| \right), \tag{28}$$

$$|\theta_{ij}| \leq \theta_{ij}^{\mathrm{max}} = \arctan \left(\left| \frac{\delta r_{ij}}{\Delta_{ij}} \right| \right), \tag{29}$$

where g_{ij} and Δ_{ij} are the coupling strength and the energy detuning between the ith and jth Floquet states. Note that we defined $g_{ii} = g_{jj} = 0$. From Eqs. (22), (27), and (29), we can estimate the lower bound of the control fidelity under such simultaneous Floquet collisions.

III. COLLISION ORDER AND GENERALIZED PERTURBATION THEORY

To find Floquet collisions, we need to search for the degeneracies of the Floquet Hamiltonian in the operation basis. Note that degeneracies not only occur between directly coupled Floquet states, but also between remote Floquet states via intermediate coupling paths between them. We compute such degeneracies by diagonalizing the Floquet Hamiltonian. If the components of two Floquet eigenstates are hybridized beyond a non-negligible fraction (threshold), we identify it as a Floquet collision. However, as shown in Eq. (3), Floquet Hamiltonians are generally infinite dimensional, and exact diagonalization is impossible with finite computational cost. However, depending on the complexity of the problem, we can perform such a diagonalization analytically using perturbation theory.

Perturbation theory gives a method for finding approximate order-by-order solutions that are slightly different from a solvable unperturbed system. In quantum mechanics, various perturbative analyses of Hamiltonian dynamics have been proposed such as Rayleigh-Schrödinger perturbation theory [74], Schrieffer-Wolff perturbation theory [44], Dyson series [75], Magnus expansion [76], average Hamiltonian theory [77], and multiscale perturbation theory [78]. We can also find several attempts of perturbative analysis on Floquet Hamiltonian in previous studies [79–81]. In this section, we propose a method for evaluating Floquet collisions with finite computational cost by applying generalized perturbation theory [50] on the Floquet Hamiltonian.

A. Generalized perturbation theory

Generalized perturbation theory [50] is formulated in superoperator notation, and hence unifies the aforementioned perturbation theories. We assume the following Hamiltonian:

$$H = K + V, \tag{30}$$

where K and V correspond to the "bare" and "perturbation" terms, respectively, and generally do not commute with each other. The goal of generalized perturbation theory is to transform the perturbation V to commute with the bare term K by finding an appropriate frame operator G to satisfy the following equation:

$$\left[e^{\mathcal{G}}(H)\, K \right] = 0, \tag{31}$$

where $\mathcal{G}(H) = [G, H]$. As a consequence of the detailed discussion about the generalized perturbation theory in Sec. A, we obtain the kth-order effective Hamiltonian $H^{(k)}$ from K and V. Note that the difference between the diagonal terms, and the off-diagonal terms, of the kth-order effective Hamiltonian correspond to the effective energy detuning $\Delta_{ij}^{(k)}$, and the effective coupling strength $g_{ij}^{(k)}$, respectively:

$$\Delta_{ij}^{(k)} = H_{ii}^{(k)} - H_{jj}^{(k)}, \tag{32}$$

$$g_{ij}^{(k)} = H_{ij}^{(k)}. \tag{33}$$

Therefore, we can verify the Floquet collisions between the ith and jth diagonal elements by a collision angle defined as

$$\theta_{ij}^{(k)} \equiv \arctan\left(\left| \frac{2 g_{ij}^{(k)}}{\Delta_{ij}^{(k)}} \right| \right). \tag{34}$$

In the following, when the kth-order effective coupling strength becomes non-negligible with respect to the kth-order effective energy detuning between them, we will call this a kth-order Floquet collision.

B. Collision order and distance in Floquet space

We identified Floquet collisions as the breakdown of the strong-dispersive conditions in the Floquet Hamiltonian, which can be detected via the collision angles defined in Eq. (34). However, the infinite dimensionality of the Floquet representation makes the exact diagonalization impossible. Hence, a systematic truncation procedure is necessary. In this subsection, we show that it is possible to verify the Floquet collisions below a certain order using only a finite-dimensional Floquet subspace Hamiltonian.

Let us define a Floquet subspace $\mathcal{S}^{(k)}(|\psi\rangle)$ spanned by Floquet states with nonzero effective couplings to a Floquet state $|\psi\rangle$ on the kth-order effective Floquet Hamiltonian $H^{(k)}$ as follows:

$$\mathcal{S}^{(k)}(|\psi\rangle) \equiv \mathrm{span}\left(H^{(k)} |\psi\rangle \right), \tag{35}$$

where "span" represents the subspace spanned by all the Floquet states in the argument. As a consequence of the detailed discussion in Sec. B, we prove that the subspace $\mathcal{S}^{(k \leq)}(|\psi\rangle)$ is encompassed in a finite dimensional Floquet subspace as

$$\mathcal{S}^{(k \leq)}(|\psi\rangle) \in \mathbb{K}_k(V, |\psi\rangle), \tag{36}$$

where $\mathbb{K}_k(V, |\psi\rangle)$ represents a kth-order Krylov subspace [82] with the perturbation V and the Floquet state $|\psi\rangle$ defined as follows:

$$\mathbb{K}_k(V, |\psi\rangle) \equiv \mathrm{span}\left(\left\{ V^j |\psi\rangle \right\}_{j=0}^{k} \right). \tag{37}$$

Suppose that the perturbation V can be expanded in the operation basis as follows:

$$V = \sum_{i,j} v_{ij} |\psi_i\rangle \langle \psi_j|. \tag{38}$$

From Eq. (38), we can define a graph G_F consisting of nodes and edges corresponding to the indices of the diagonal and the nonzero off-diagonal elements of the perturbation V, respectively. The kth power of V is decomposed as follows:

$$V^k = \sum_{\mathbf{l}_i^{(k)}} \left\{ \left(\prod_{(l,m) \in \mathbf{l}^{(k)}} v_{lm} \right) |\psi_i\rangle \langle \psi_i| \right\}$$
$$+ \sum_{\mathbf{w}_{i \neq j}^{(k)}} \left\{ \left(\prod_{(l,m) \in \mathbf{w}^{(k)}} v_{lm} \right) |\psi_i\rangle \langle \psi_j| \right\}, \tag{39}$$

where $\mathbf{l}_i^{(k)}$ and $\mathbf{w}_{i \neq j}^{(k)}$ correspond to a length-k loop around a node i and a length-k walk between nodes i and j on the graph G_F, respectively. The graphical interpretation of the

perturbation is sometimes called the path-sum approach [83,84]. For verifying up to the kth-order Floquet collisions between a pair of Floquet states, we need to calculate up to the kth-order energy shifts and effective coupling strengths between them. From Eq. (39), we can find that kth-order energy shifts and effective couplings correspond to the length-k loop around the Floquet states and the length-k walk between them, respectively. As shown in Fig. 3(a), such loops and walks are encompassed in the region within the distance $d = \lfloor k/2 \rfloor$ from both Floquet states. Thus, to verify up to kth-order Floquet collisions caused on a Floquet state, we need to apply the same procedure for all Floquet states at distance k from the Floquet state. Such a process is encompassed in the region within distance $d = \lfloor 3k/2 \rfloor$ from the Floquet state on the Floquet subspace Hamiltonian.

Finally, we discuss the search and verification of all possible Floquet collisions for a given Floquet Hamiltonian. The periodicity of the Floquet Hamiltonian indicates that the Floquet collisions that occur between $|x, \vec{\mathbf{n}}_x\rangle$-$|y, \vec{\mathbf{n}}_y\rangle$ also occur between $|x, \vec{\mathbf{n}}_x + \vec{\mathbf{r}}\rangle$-$|y, \vec{\mathbf{n}}_y + \vec{\mathbf{r}}\rangle$ for any translation operation $\vec{\mathbf{r}}$ to the BZ. Therefore, all Floquet collisions that occur in the Floquet Hamiltonian can be ascertained by verifying only the Floquet collisions that occur in the $\vec{\mathbf{0}}$th BZ.

C. Collision order and distance in real space

In Sec. III B, we laid out a correspondence between collision order and distance on the Floquet Hamiltonian. For applications to quantum systems involving many qubits, it is also crucial to know the correspondence between collision order and distance in real space, in order to truncate our model down to the optimal complexity.

First, we note that Floquet states at distance d do not always experience dth-order Floquet collisions. As an example, suppose two isolated qubits individually irradiated by microwave drives as shown in Fig. 3(b). Despite no qubit-qubit interaction, there is a walk of distance 2 between $|0, 0; 0, 0\rangle$ and $|1, 1; -1, -1\rangle$ mediated by $|0, 1; 0, -1\rangle$ and $|1, 0; -1, 0\rangle$ on the Floquet Hamiltonian. However, they cannot collide with each other in any parameter regime, because the effective couplings between them caused by the two coupling walks always cancel each other out.

Such a relationship can be written more generally as follows. Floquet states are coupled to each other by off-diagonal terms in the Floquet Hamiltonian. Each off-diagonal term corresponds to an interaction in real space according to Eq. (5). Consider an arbitral x-body interaction H_I acting on the qubits $\{Q_i\}_{i=1}^x$. The interaction then corresponds to node $\{Q_i\}_{i=1}^x$ and the edge that joins them
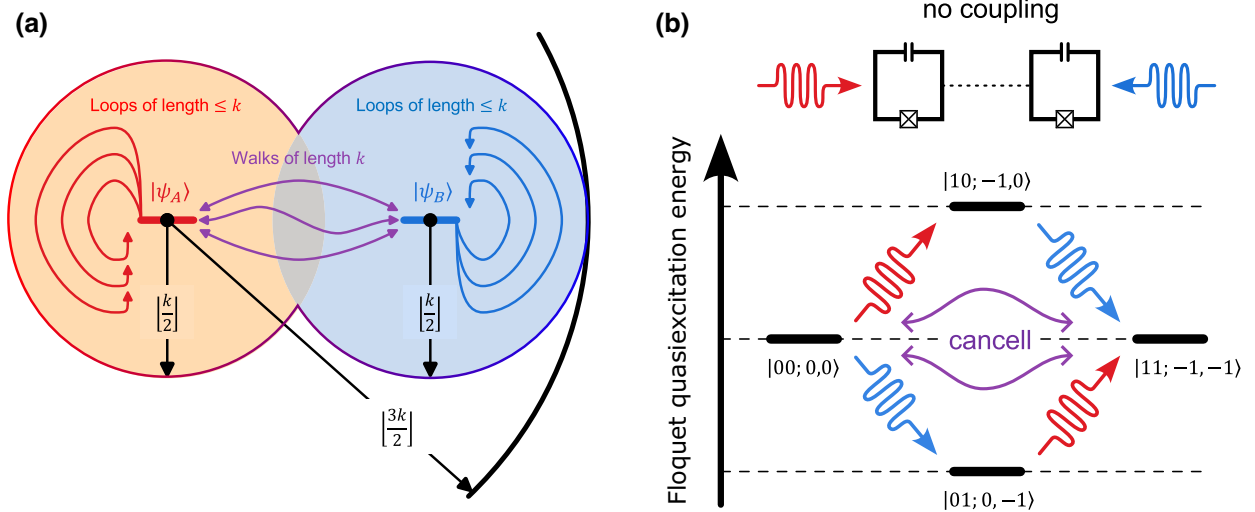

FIG. 3. (a) Graphical interpretation of the kth-order perturbations acting on the Floquet states $|\psi_{A,B}\rangle$. A loop of length k around Floquet states $|\psi_{A,B}\rangle$ and a walk of length k between them on the Floquet Hamiltonian correspond to kth-order Floquet quasi-excitation energy shifts and effective coupling, respectively. To verify the kth-order Floquet collision, we compare the Floquet quasiexcitation energy detuning, accounting for up to kth-order energy shifts, to the kth-order effective coupling strength. Such loops and walks are contained in a region within distance $d \leq \lfloor k/2 \rfloor$ of each state, such that we can use the Floquet subspace Hamiltonian corresponding to this region to verify the kth-order Floquet collision with finite computational cost. All Floquet collisions up to the kth-order caused on the Floquet state $|\psi_A\rangle$ include only Floquet collisions with the Floquet states within distance $d \leq k$. Thus, all Floquet collisions caused on $|\psi_A\rangle$ can be calculated with the Floquet subspace Hamiltonian corresponding to the region within distance $d \leq \lfloor 3k/2 \rfloor$ from $|\psi_A\rangle$ in the Floquet Hamiltonian. (b) The circuit and the corresponding low-excitation Floquet energy-level diagram of two isolated transmon qubits irradiated by independent microwave drives. Even though there is no qubit-qubit interaction, there is a walk of distance 2 between states $|0, 0; 0, 0\rangle$ and $|1, 1; -1, -1\rangle$ mediated by $|0, 1; 0, -1\rangle$ and $|1, 0; -1, 0\rangle$ on the Floquet Hamiltonian. However, the effective couplings between them, mediated by two coupling walks, always cancel each other out.

all. Let $\{H_I\}$ now be the pair of such interactions that relay a particular walk between particular Floquet states on the Floquet Hamiltonian. Consider a graph G_R that consists of all the nodes and edges corresponding to the interactions $\{H_I\}$. If G_R is not a connected graph, such a walk must be ignored because it will always cancel out with other similar walks. In the following, such a walk is called an invalid walk and the converse is called a valid walk. We will also refer to the qubits relevant to the nodes of the connected graph G_R as the qubits involved in the walk.

Consider a qubit lattice where qubits couple via two-body interactions under strong-dispersive conditions. A valid walk simultaneously involving qubits in a distance d on the lattice must relay at least d two-body interactions, and thus always has a length d or more. From the discussion in Sec. III B, kth-order Floquet collisions caused on a Floquet state are complete within a subspace of distance $d = \lfloor 3k/2 \rfloor$ from the state. Thus, we can say that the only qubits that can simultaneously be involved in a kth-order Floquet collisions involving a qubit are those within a distance $d = \lfloor 3k/2 \rfloor$ from that qubit.

IV. COLLISION ANALYSIS AND COMPUTATIONAL COMPLEXITY

In Sec. III, we have shown that for the analysis of Floquet collisions it is sufficient to work with a truncated finite-dimensional Floquet subspace Hamiltonian in the $\vec{0}$th BZ. However, the dimension of the $\vec{0}$th BZ scales exponentially with the number of qubits, making its analysis computationally difficult. In this section, we propose a collision analysis method that scales linearly with the number of qubits by considering the lattice structure of multiqubit systems. In the following, we consider the case where the operation basis can be expressed as a tensor product state for each qubit. Note that we can also treat the cases with an entangling operation basis using Algorithm 3 in Sec. D.

A. Collision analysis for general qubit lattice

Based on the discussions of the previous sections, we summarize our Floquet-based collision analysis for the general qubit lattice in Algorithm 1. Consider the

computational complexity $C_1(k, n, d, m)$ of kth-order collision analysis on a general n-qudit lattice, with all-to-all connectivity, where each qudit has d levels and is irradiated with at most m different microwave drive frequencies. The corresponding $\vec{0}$th BZ of the Floquet Hamiltonian has dimension $\mathcal{O}(d^n)$. There are $\mathcal{O}((m+n)^{\lfloor 3k/2 \rfloor})$ nodes within $\lfloor 3k/2 \rfloor$ distance from a particular node in the Floquet Hamiltonian, which becomes the dimension of the Floquet subspace Hamiltonian to compute all possible kth-order Floquet collisions. The leading term of the computational complexity $C_1(k, n, d, m)$ comes from the kth-order perturbative diagonalization of the Floquet subspace Hamiltonian. The computational complexity of the kth-order perturbative diagonalization of an $N \times N$-dimensional matrix is $\mathcal{O}(2^k N^3)$. Therefore, the total computational complexity $C_1(k, n, d, m)$ is given as follows:

$$C_1(k, n, d, m) = \mathcal{O}\left(2^k \left\{ d^n (m+n)^{\lfloor \frac{3k}{2} \rfloor} \right\}^3 \right). \quad (40)$$

From Eq. (14), we can find that the gate errors caused by Floquet collisions depend mainly on the subspace spanned by the colliding Floquet states. Therefore, the Floquet collisions of the computational Floquet states deteriorate the gate fidelity, and we can apply $d = 2$ to Eq. (40). Because the dimension of the $\vec{0}$th BZ increases exponentially with the number of qubits, Algorithm 1 is feasible only for a limited number of qubits.

B. Collision analysis for sparse qubit lattice

Promising error-correction codes, such as the surface code [85–87] and the color code [88], require qubits to be arranged in a periodic lattice structure with sparse connectivity. The distance between qubits can be defined by taking the qubits as nodes and the nonzero exchange interaction between them as edges. As discussed in Sec. III C, only qubits in the sublattice within a distance $d = \lfloor 3k/2 \rfloor$ from a particular qubit can be involved in up to kth-order Floquet collisions affecting the qubit. Therefore, we can verify all possible kth-order Floquet collisions in the whole lattice by analyzing the corresponding sublattice around each qubit sequentially. Thus, the collision analysis for the sparse qubit lattice is summarized in Algorithm 2.

1: Apply the discrete Fourier expansion to the target Hamiltonian as in Eq. (3)
2: Construct a Floquet Hamiltonian from the expansion coefficients of the discrete Fourier series as Eq. (5)
3: Represent the Floquet Hamiltonian in the operation basis
4: Convert the matrix representation of the Floquet Hamiltonian into a graph
5: Around each node of interest in the graph, extract a subgraph within radius of $\lfloor 3k/2 \rfloor$.
6: Perform $(k-1)$th-order diagonalization of the Floquet subspace Hamiltonian corresponding to the subgraph as Eq. (A14)
7: Calculate the collision angle between all states of interest in the $\vec{0}$th BZ relative to the other states in the $(k-1)$th-order diagonalized Hamiltonian as Eq. (34)
8: Identify the states with collision angles greater than a threshold as causing kth-order Floquet collisions

---

Algorithm 1. Collision analysis for general qubit lattice

1: **for** center qubit from the qubit lattice **do**
2:     Extract a sublattice including only the qubits within distance $\lfloor 3k/2 \rfloor$ from the center qubit
3:     Construct a subspace Hamiltonian H^{sub} corresponding to the sublattice
4:     Verify kth-order Floquet collisions involving the center qubit with Algorithm 1
5:     Remove the center qubit from the qubit lattice

Algorithm 2.   Collision analysis for sparse qubit lattice

Consider the computational complexity $C_2(k,n,d,m,r)$ of kth-order collision analysis on a sparse n-qudit lattice of maximum degree r, where each qudit has d levels and is irradiated with at most m different microwave drive frequencies. The sublattice needed to compute the kth-order frequency collisions caused at each qubit contains $\mathcal{O}(r^{\lfloor 3k/2 \rfloor})$ qubits. We apply Algorithm 1 to all sublattices. Therefore, the total computational complexity $C_2(k,n,d,m,r)$ is given as follows:

$$C_2(k,n,d,m,r) = nC_1(k, r^{\lfloor 3k/2 \rfloor}, d, m, r)$$

$$= \mathcal{O}\left(n2^k \left\{ d^{r^{\lfloor \frac{3k}{2} \rfloor}} (m+r)^{\lfloor \frac{3k}{2} \rfloor} \right\}^3 \right), \quad (41)$$

which is linear with respect to the number of qudits n. Similar to Eq. (40), we can apply $d \to 2$ when dealing only with fidelity deterioration caused by the Floquet collisions.

V. DEMONSTRATION

In this section, we apply our Floquet-based collision analysis to relevant experimental systems and protocols. First, we apply Algorithm 1 to CR gates [41–43] on isolated two- or three-transmon systems, then calculate analytical solutions of the collision bounds, which have been studied numerically so far [49]. Next, we apply Algorithm 2 to a heavy-hexagon code [17,52] for quantitative estimation of the difficulty of system-frequency allocation.

A. Model

We first describe our model of fixed-frequency transmon qubits [89,90] coupled via exchange interactions as follows:

$$H = \sum_i \left\{ \omega_i a_i^\dagger a_i + \frac{\alpha_i}{2} a_i^\dagger a_i^\dagger a_i a_i \right\}$$

$$+ \sum_{i,j} \left\{ J_{ij} \left(a_i^\dagger + a_i \right) \left(a_j^\dagger + a_j \right) \right\}$$

$$+ \sum_k \left\{ \Omega_k \cos\left(\omega_{dk} t + \phi_k \right) \left(a_{t_k}^\dagger + a_{t_k} \right) \right\}, \quad (42)$$

where ω_i, α_i, and J_{ij} are qubit frequencies, anharmonicities, and pairwise exchange interactions. Moreover, Ω_k, ω_{dk}, and ϕ_k are the amplitude, frequency, and phase of the

kth-microwave drive on the target qubit t_k, respectively. The annihilation operator for the ith qubit is shown as a_i.

B. Cross-resonance gate on an isolated-transmon system

In this subsection, we apply Algorithm 1 to Floquet collisions of CR gates on isolated few-transmon systems, then present analytical solutions up to second-order in perturbation. We first consider an isolated CR gate consisting of control and target qubits. Next, we present a generalization with a third spectator qubit [36].

To implement the CR gate, the control qubit is irradiated with a microwave drive resonant with the dressed frequency of the target qubit. Following Eq. (42), the system
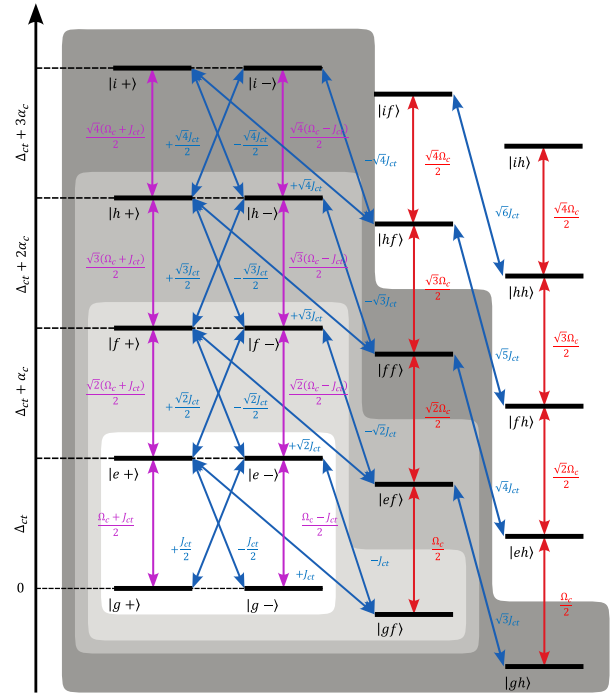

FIG. 4.   Floquet energy-level diagram of the CR Hamiltonian [Eq. (43)]. For simplicity, the CR drive frequency is set to the bare target qubit frequency ω_t. Also, the BZ index of the Floquet states is omitted. The gray regions represent the distance from the computational states $\{|g\pm\rangle, |e\pm\rangle\}$, respectively, with darker shades further away. Although the $|x\pm\rangle$ states appear to be degenerate for $x \in [g, e, f, h, i \cdots]$, they are in fact detuned by a second-order energy shift originating from the CR interaction, preserving the strong-dispersive condition.

TABLE I.   Analytical solution of Floquet collisions for the two-transmon CR system up to second-order in perturbation. The first column represents the degenerate Floquet state pairs in the operation basis, where we omitted the BZ index for simplicity. The second column shows the labels for the frequency collisions under which the collision factors of the corresponding Floquet collisions diverge as in Table III. From the second column, we find that multiple Floquet state pairs can become degenerate for a given frequency condition. The third column shows the order of the Floquet collisions defined in Sec. III B. The fourth column shows the collision factors, i.e., the linearized collision angles. We can verify Floquet collisions by checking whether the collision factors are sufficiently smaller than 1.

$|c,t\rangle$	Type	Order	Collision factor
$|g\pm\rangle \leftrightarrow |e\pm\rangle$	1	1	$\dfrac{J_{ct} \pm \Omega_c}{2\Delta_{ct}}$
$|g\pm\rangle \leftrightarrow |e\mp\rangle$	1	1	$\dfrac{J_{ct}}{2\Delta_{ct}}$
$|gf\rangle \leftrightarrow |e\pm\rangle$	3	1	$\dfrac{J_{ct}}{\Delta_{ct} - \alpha_t}$
$|e\pm\rangle \leftrightarrow |f\pm\rangle$	3	1	$\dfrac{J_{ct} \pm \Omega_c}{\sqrt{2}\,(\Delta_{ct} + \alpha_c)}$
$|e\pm\rangle \leftrightarrow |f\mp\rangle$	3	1	$\dfrac{J_{ct}}{\sqrt{2}\,(\Delta_{ct} + \alpha_c)}$
$|g+\rangle \leftrightarrow |g-\rangle$	3	2	$\dfrac{\Delta_{ct}J_{ct}(\alpha_c + \alpha_t)}{2\Omega_c(\Delta_{ct} + \alpha_c)(\Delta_{ct} - \alpha_t)}$
$|g\pm\rangle \leftrightarrow |gf\rangle$	1,3	2	$\pm\dfrac{\Omega_c J_{ct}}{4\alpha_t}\left(\dfrac{1}{\Delta_{ct} - \alpha_t} + \dfrac{1}{\Delta_{ct}}\right)$
$|g\pm\rangle \leftrightarrow |f\pm\rangle$	1,2,3	2	$\dfrac{\sqrt{2}\Omega_c\alpha_c(\Omega_c \pm 2J_{ct})}{8\Delta_{ct}(\Delta_{ct} + \alpha_c)(2\Delta_{ct} + \alpha_c)}$
$|g\pm\rangle \leftrightarrow |f\mp\rangle$	1,2,3	2	$\pm\dfrac{\sqrt{2}\Omega_c\alpha_c J_{ct}}{4\Delta_{ct}(\Delta_{ct} + \alpha_c)(2\Delta_{ct} + \alpha_c)}$
$|e+\rangle \leftrightarrow |e-\rangle$	3,8	2	$\dfrac{\Delta_{ct}J_{ct}(\alpha_c + \alpha_t)}{2\Omega_c(\Delta_{ct} - \alpha_c)(\Delta_{ct} - \alpha_t)}$
$|e\pm\rangle \leftrightarrow |ef\rangle$	1,3,9	2	$\pm\dfrac{\Omega_c J_{ct}}{2\alpha_t}\left(\dfrac{1}{\Delta_{ct} + \alpha_c} + \dfrac{1}{\Delta_{ct} + \alpha_c - \alpha_t} - \dfrac{2\Delta_{ct} - \alpha_t}{2\Delta_{ct}(\Delta_{ct} - \alpha_t)}\right)$
$|e\pm\rangle \leftrightarrow |h\pm\rangle$	3,10,11	2	$\dfrac{\sqrt{6}\Omega_c\alpha_c(\Omega_c \pm 2J_{ct})}{8(\Delta_{ct} + \alpha_c)(\Delta_{ct} + 2\alpha_c)(2\Delta_{ct} + 3\alpha_c)}$
$|e\pm\rangle \leftrightarrow |h\mp\rangle$	3,10,11	2	$\pm\dfrac{\sqrt{6}\Omega_c\alpha_c J_{ct}}{4(\Delta_{ct} + \alpha_c)(\Delta_{ct} + 2\alpha_c)(2\Delta_{ct} + 3\alpha_c)}$

Hamiltonian is

$$H = \sum_{i\in[c,t]}\left\{\omega_i a_i^\dagger a_i + \frac{\alpha_i}{2}a_i^\dagger a_i^\dagger a_i a_i\right\} + J_{ct}\left(a_c^\dagger + a_c\right)\left(a_t^\dagger + a_t\right)$$
$$+ \Omega_c\cos(\tilde{\omega}_t t)\left(a_c^\dagger + a_c\right), \tag{43}$$

with indices "c" and "t" referring to the control and the target qubits, respectively. The drive frequency should be set to the *dressed* target frequency $\tilde{\omega}_t$ found perturbatively up to $O(J_{ct}^4)$ as

$$\tilde{\omega}_t \approx \omega_t - \frac{J_{ct}^2}{\Delta_{ct}} + \frac{(\alpha_c + \alpha_t)J_{ct}^2}{(\Delta_{ct} + \alpha_c)(\Delta_{ct} - \alpha_t)}, \tag{44}$$

where $\Delta_{ct} \equiv \omega_c - \omega_t$. Moreover, for the spectator problem, we consider a third transmon qubit, coupled to the control, denoted by index s.

Under such a CR drive scheme, a controlled-X rotation occurs in the computational subspace of the target qubit depending on the state of the control qubit. We therefore choose the Floquet operation basis as

$$|c,t;n\rangle = |c\rangle \otimes |t;n\rangle, \tag{45}$$

$$|\pm;n\rangle = \frac{1}{\sqrt{2}}(|g;n\rangle \pm |e;n-1\rangle), \tag{46}$$

with $c \in [g,e,f,\ldots]$, $t \in [+,-,f,\ldots]$, and the BZ index $n \in \mathbb{Z}$. In the following, we omit BZ index n for simplicity.

Figure 4 shows the Floquet energy-level diagram in the operation basis. Using Algorithm 1, we verify up to second-order Floquet collisions involving the computational basis $\{|g,\pm\rangle, |e,\pm\rangle\}$. First, we extract the subgraph consisting of nodes within a distance of 3 from the computational subspace. Next, we apply perturbative

TABLE II. Analytical solution of Floquet collisions for the three-transmon CR system with a control spectator qubit up to second order. We show the Floquet state pairs, corresponding frequency collisions, collision orders, and collision factors for various Floquet collisions similar to Table I.

$|c,t,s\rangle$	Type	Order	Collision factor
$|g \pm e\rangle \leftrightarrow |e \pm g\rangle$	1	1	$-\dfrac{J_{cs}}{\Delta_{cs}}$
$|g \pm f\rangle \leftrightarrow |e \pm e\rangle$	3	1	$\dfrac{\sqrt{2}J_{cs}}{\alpha_s - \Delta_{cs}}$
$|e \pm e\rangle \leftrightarrow |f \pm g\rangle$	3	1	$-\dfrac{\sqrt{2}J_{cs}}{\alpha_c + \Delta_{cs}}$
$|g \pm g\rangle \leftrightarrow |g \pm e\rangle$	1,5	2	$\dfrac{\Omega_c J_{cs}}{4\Delta_{st}}\left(\dfrac{1}{\Delta_{ct}} + \dfrac{1}{\Delta_{cs}}\right)$
$|g \pm e\rangle \leftrightarrow |g \pm f\rangle$	1,3,6	2	$\dfrac{\sqrt{2}\Omega_c J_{cs}}{\Delta_{st} + \alpha_s}\left(\dfrac{1}{\Delta_{ct}} - \dfrac{1}{\Delta_{sc} + \alpha_s}\right)$
$|g \pm e\rangle \leftrightarrow |f \pm g\rangle$	1,3,7	2	$\dfrac{\sqrt{2}\Omega_c\alpha_c J_{cs}}{4(\Delta_{ct} + \Delta_{cs} + \alpha_c)}\left(\dfrac{1}{\Delta_{ct}(\Delta_{ct} + \alpha_c)} + \dfrac{1}{\Delta_{cs}(\Delta_{cs} + \alpha_c)}\right)$
$|e \pm g\rangle \leftrightarrow |e \pm e\rangle$	1,3,5	2	$\dfrac{\Omega_c J_{cs}}{4\Delta_{st}}\left(\dfrac{2}{\Delta_{cs} + \alpha_c} + \dfrac{2}{\Delta_{ct} + \alpha_c} - \dfrac{1}{\Delta_{cs}} - \dfrac{1}{\Delta_{ct}}\right)$
$|e \pm e\rangle \leftrightarrow |e \pm f\rangle$	1,3,6,9	2	$\sqrt{2}\Omega_c J_{cs}\left(\dfrac{1}{(\Delta_{st} + \alpha_s)(\Delta_{cs} + \alpha_c - \alpha_s)} - \dfrac{1}{4(\Delta_{cs} - \alpha_s)(\Delta_{st} + \alpha_s)}\right.$ $\left. - \dfrac{1}{2(\Delta_{ct} + \alpha_c)(\Delta_{cs} + \alpha_c - \alpha_s)} - \dfrac{1}{4\Delta_{ct}(\Delta_{st} + \alpha_s)}\right)$
$|e \pm e\rangle \leftrightarrow |h \pm g\rangle$	3,10,12	2	$\dfrac{\sqrt{6}\Omega_c\alpha_c J_{cs}}{4(\Delta_{ct} + \Delta_{cs} + 3\alpha_c)}\left(\dfrac{1}{(\Delta_{ct} + \alpha_c)(\Delta_{ct} + 2\alpha_c)} + \dfrac{1}{(\Delta_{cs} + \alpha_c)(\Delta_{cs} + 2\alpha_c)}\right)$

diagonalization on a Floquet subspace Hamiltonian reconstructed from the subgraph. Finally, we calculate collision factors: fractions of the off-diagonal terms to the detuning between the diagonal terms as linearized collision angles between the corresponding Floquet states. For simplicity, we omitted terms $\mathcal{O}(J_{ct}^x\Omega^y)$ for $x + y \geq 3$ in the following.

Table I shows the pairs of Floquet states involved in up to second-order Floquet collisions and their corresponding collision factors. Here, from the discussion in Sec. IV, we chose only the pairs with at least one computational state. We also calculate the case with a spectator qubit coupled to the control qubit and show the results in Table II, where ω_s and J_{cs} are the spectator qubit frequency and the control-spectator coupling strength, respectively. We show only Floquet collisions with the factor of $\mathcal{O}(J_{ct}^x J_{cs}^y \Omega^z)$ with $x + y < 2$ and $z < 3$ for brevity, but in principle our analysis can provide further higher-order Floquet collisions. From Tables I and II, we find several frequency conditions under which some of the collision factors diverge. They correspond to conventional frequency collisions [36, 39,49]. We have summarized the frequency collisions in Table III and given the properties of each in Appendix E.

Tables I and II also show for which type of frequency collisions the collision factors diverge and the corresponding perturbation order in the effective coupling strength between Floquet states. The collision factor diverges

when the strong-dispersive condition is completely broken down, i.e., two of the Floquet states are precisely degenerate, in the valid walk between the target Floquet states on the Floquet Hamiltonian. Thus, as shown in Tables I and II, the first-order Floquet collisions with no mediating Floquet states have only one frequency collision, whereas the second-order Floquet collisions with multiple mediating Floquet states have multiple frequency collisions.

The frequency collisions in Table III agree mostly with the results in the previous studies [36,49]. The differences from the previous studies are type 4 and type 8. Type 4 was proposed in Refs. [39,49] as an empirical straddling regime frequency allocation requirement for the coupled-transmon systems to have stronger CR interaction. We, however, note that the type-4 collision does not correspond to an actual frequency collision under our Floquet-based collision analysis. On the other hand, type 8 is a new frequency collision not mentioned previously [36,39,49]. As shown in Table I, type 8 appears only in the Floquet collision between $|e+\rangle$ and $|e-\rangle$ states, which can be understood in terms of the effective CR Hamiltonian [43]:

$$H_{\mathrm{CR}} = \Omega_{ZX}\frac{ZX}{2} + \Omega_{IX}\frac{IX}{2}. \tag{47}$$

TABLE III. Analytical solutions of the frequency collisions where the corresponding collision factors cited in Tables I and II diverges. The labels used here follow the previous empirical classification of the frequency collisions [39,49]. We note, however, that the previously labeled type-4 collision does not correspond to an actual frequency collision under our Floquet-based collision analysis. It is an empirical frequency allocation requirement to have control-target detuning in the straddling regime to have stronger CR interaction. On the other hand, type 8 is an alternative frequency collision, which has not been reported in the previous studies. Type 8 is caused by the mutual cancellation of entanglement interaction and quantum crosstalk in the CR drive. Detailed discussion is found in Sec. V B.

Type	Frequency condition	Order
1	$\Delta_{ct} = 0$	1
	$\Delta_{cs} = 0$	1
2	$2\Delta_{ct} + \alpha_c = 0$	2
3	$\Delta_{ct} + \alpha_c = 0$	1
	$\Delta_{ct} - \alpha_t = 0$	1
	$\Delta_{cs} + \alpha_c = 0$	1
	$\Delta_{cs} - \alpha_s = 0$	1
5	$\Delta_{st} = 0$	2
6	$\Delta_{st} + \alpha_s = 0$	2
	$\Delta_{st} - \alpha_t = 0$	2
7	$\Delta_{ct} + \Delta_{cs} + \alpha_c = 0$	2
8	$\Delta_{ct} - \alpha_c = 0$	2
9	$\Delta_{ct} + \alpha_c - \alpha_t = 0$	2
	$\Delta_{cs} + \alpha_c - \alpha_s = 0$	2
10	$\Delta_{ct} + 2\alpha_c = 0$	2
	$\Delta_{cs} + 2\alpha_s = 0$	2
11	$2\Delta_{ct} + 3\alpha_c = 0$	2
12	$\Delta_{ct} + \Delta_{cs} + 3\alpha_c = 0$	2

The energy detuning between the $|e+\rangle$ and $|e-\rangle$ states is expressed as $\Omega_{IX} - \Omega_{ZX} \propto \Delta_{ct} - \alpha_c$, and thus the collision factor is inversely proportional to $\Delta_{ct} - \alpha_c$.

From our perturbative estimates for the collision factors, we can also provide analytical bounds on fidelity degradation for a given Floquet collision as Sec. II B. Our analytical collision factors would provide more flexible and precise system-frequency allocation. From Tables I and II, we find that the collision factors depend not only on the qubit frequency, anharmonicity, and the coupling strength, but also on the microwave drive amplitude. It suggests drive-induced Floquet collisions and can explain why the CR gate fidelity and execution time are limited in the previous experiments [29,91]. More rigorous analysis on adiabatic conditions for the Floquet collisions would enable faster CR gates.

The discussion so far provides an analytical formulation of (i) mechanism, (ii) type, and (iii) bounds of frequency collisions in two- or three-qubit CR systems. We can also perform numerical Floquet simulations to visualize the Floquet collisions. Figure 5 shows the simulation results of Algorithm 1 for a two-qubit CR gate with fixed CR

drive amplitude of $\Omega_c/2\pi = 30$ MHz while sweeping the control-target detuning $\Delta_{ct}/2\pi$ between -1 to 1 GHz. The top panel shows the Floquet quasiexcitation energies of the system. As shown in the figure, some of the Floquet quasiexcitation energies change linearly with the detuning sweep and exhibit avoided crossings that we refer to as Floquet collisions. The second and third rows of the figure show the maximum values of the collision angles corresponding to first- and second-order Floquet collisions, respectively. Note that we plotted collision angles only for Floquet collisions involving the computational subspace. The red and black vertical lines label the underlying first- and second-order frequency collisions, respectively. Under the first-order frequency collisions, we find type 1 and type 3. Among the type-3 cases, the case where the *ef*-transition frequency of the control qubit is degenerate to the *ge*-transition frequency of the target qubit has larger collision bound than the opposite case. This is because the former corresponds to $|e\pm\rangle$-$|f\pm\rangle$ Floquet collision whose collision factor is proportional to Ω_c, while the latter corresponds to a $|gf\rangle$-$|e\pm\rangle$ Floquet collision whose collision factor is proportional to J_{ct}. Under the second-order frequency collisions, we find types 2, 8, 9, 10, 11 in addition.

Figure 6 shows the simulation results of Algorithm 1 for a CR drive on two (a),(b) or three (c) qubits with two-dimensional (2D) sweep of system parameters. One of the sweeping system parameters is always the control-target detuning $\Delta_{ct}/2\pi$ from -1 to 1 GHz. In each figure, the top and bottom figures show grayscale plots of the maximum collision angles corresponding to first- and second-order Floquet collisions, respectively. The colored lines and their labels represent the corresponding frequency or Floquet collisions.

In Fig. 6(a), we sweep the CR drive amplitude $\Omega_c/2\pi$ from -100 to 100 MHz in addition to the control-target detuning. The first-order collision angle (top panel) reveals one type-1 and two type-3 frequency collisions the same as Fig. 5. The width of the type 1 ($\Delta_{ct} = 0$) and one of the type-3 frequency collisions ($\Delta_{ct} + \alpha_c = 0$) increases with stronger drive amplitude in agreement with Table I, where the collision factors are proportional to Ω_c. The other type-3 frequency collision ($\Delta_{ct} - \alpha_t = 0$), corresponding to the Floquet collision $|gf\rangle \leftrightarrow |e\pm\rangle$, is independent of the CR drive amplitude. Second-order collision angles (bottom panel) exhibit both an increase and decrease in the linewidth as well as a Stark shift in frequency collisions with increasing CR drive amplitude. Decreasing linewidth is observed only for type 8, i.e., Floquet collisions between $|g+\rangle$ ($|e+\rangle$) and $|g-\rangle$ ($|e-\rangle$), where the collision factor in Table I is inversely proportional to Ω_c, and therefore occurs independently of Δ_{ct} at $\Omega_c = 0$. This is due to the static-ZZ interaction, causing the frequency of the target qubit to depend on the control qubit. When the CR drive amplitude is 0, in the operation basis, $|g+\rangle$ ($|e+\rangle$) and
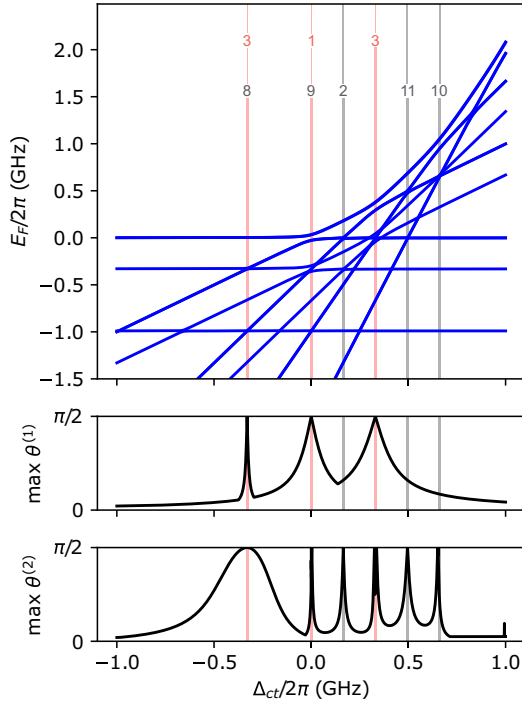
FIG. 5.   Numerical simulations of Algorithm 1 for a two-qubit CR system while sweeping the control-target detuning $\Delta_{ct}/2\pi$ from -1 to 1 GHz. Qubits anharmonicity and qubit-qubit coupling are set to -330 and 3.8 MHz, respectively. The top panel shows the Floquet quasiexcitation energies in the Floquet subspace generated for searching up to the second-order Floquet collisions. As a function of detuning, certain Floquet quasiexcitation energies shift and anticross with each other. The middle and lower panels represent the maximum collision angles between the Floquet state pairs corresponding to first- and second-order Floquet collisions, respectively. The vertical lines and their labels represent the frequency collisions shown in Table III.

$|g-\rangle$ ($|e-\rangle$) have no energy gap caused by the CR drive and are therefore degenerate.

In Fig. 6(b), we add a rotary-tone drive [42,51] into the system and sweep its amplitude $\Omega_t/2\pi$ from -5 to 5 MHz. A rotary-tone drive is a kind of spin-locking technique, which is a resonant drive to the target qubit employed to eliminate unwanted error terms having an anticommutative relation to IX in the effective CR Hamiltonian. The top panel shows that the frequency collision, corresponding to the Floquet collision between $|gf\rangle$ and $|e\pm\rangle$, splits with increasing $|\Omega_t|$, as a result of drive-induced Stark shift of the Floquet quasiexcitation energies of states $|e\pm\rangle$. The bottom panel shows that the two peaks in the collision angles, corresponding to Floquet collisions between $|g+\rangle$ ($|e+\rangle$) and $|g-\rangle$ ($|e-\rangle$), are strongly dependent on Ω_t. The rotary tone causes the Floquet quasiexcitation energies of $|g\pm\rangle$ and $|e\pm\rangle$ to shift, where the detuning

obeys

$$\Delta_{g\pm} = \Omega_t + \Omega_{IX} + \Omega_{ZX}, \qquad (48)$$

$$\Delta_{e\pm} = \Omega_t + \Omega_{IX} - \Omega_{ZX}, \qquad (49)$$

with Ω_{ZX} and Ω_{IX} being the ZX and IX term in the CR effective Hamiltonian [Eq. (47)]. In the bottom panel, the red and blue curves correspond to $\Delta_{g\pm} = 0$ and $\Delta_{e\pm} = 0$, respectively, which are well aligned with the peaks. Therefore, our Floquet analysis clarifies the role of the rotary tone as a technique to artificially widen the detuning between $|g+\rangle$ ($|e+\rangle$) and $|g-\rangle$ ($|e-\rangle$), which suppresses the type-8 collision due to static-ZZ interaction.

In Fig. 6(c), we introduce a spectator qubit, coupled only to the control qubit, and sweep the control-spectator detuning $\Delta_{cs}/2\pi$ from -1 to $+1$ GHz. In the top panel, the vertical and horizontal peaks correspond to independent first-order Floquet collisions between the control-spectator and control-target qubits, respectively. This is the case as first-order Floquet collisions involve only nearest-neighboring qubits following Sec. III C. The bottom panel, however, shows diagonal peaks corresponding to the frequency collisions between the target and spectator qubits, allowed in second-order Floquet collisions. Moreover, the red diagonal lines corresponding to types 5, 6, 7, and 12, which are well aligned with the diagonal peaks. An interesting observation is that the peaks anticross each other at the intersections, which we refer to as "collision avoided crossing." As discussed in Sec. II B, when multiple Floquet collisions involve the same Floquet state simultaneously, the collision conditions are derived by diagonalizing the subspace spanned by the colliding Floquet states. The frequency collisions shown in Table III do not assume the simultaneous Floquet collisions, so the red diagonal lines overlook the collision avoided crossings. These observations suggest that frequency allocation for large-scale quantum processors requires more involved analysis compared to the previous plans derived based on small-scale system considerations [39,49].

C. Syndrome extraction on a heavy-hexagon lattice

In Sec. V B, we analyzed the CR gate on an isolated system, i.e., a monomodal drive on a system with a few number of qubits. In this subsection, we analyze the heavy-hexagon code [17,52], which is a subsystem stabilizer code [92–94], with qubits forming a heavy-hexagonal lattice as in Fig. 7(a). We note that the Floquet analysis is substantially more involved due to the multimodal nature of the problem.

In the heavy-hexagon code, qubits belong to one of the data ($\mathcal{D}$), ancilla ($\mathcal{A}$), or flag ($\mathcal{F}$) qubits shown as yellow, white, or blue circles, respectively. The data qubits are aligned in a square lattice, as shown in Fig. 7(a). Let us assume a $d \times d$ square lattice consisting of the data
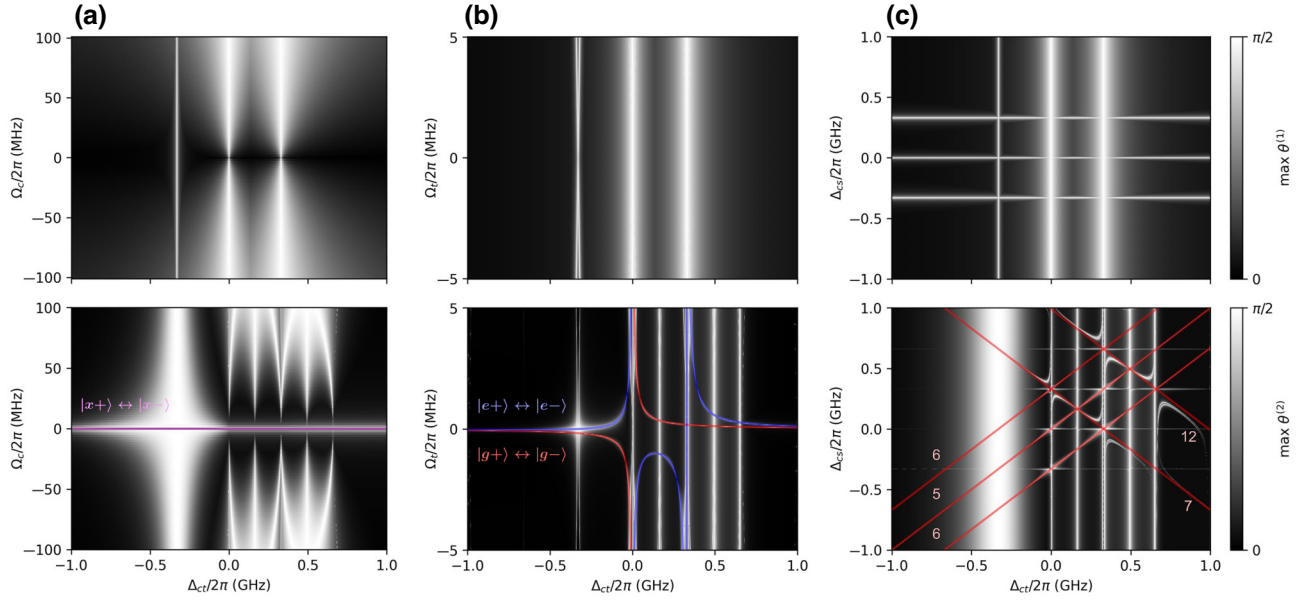
FIG. 6.   Numerical simulations of Algorithm 1 for a CR drive on two (a),(b) or three (c) transmon system with 2D sweep of system parameters. One of the sweeping system parameters is always control-target detuning $\Delta_{ct}/2\pi$ from -1 to 1 GHz. Qubit-qubit coupling strength and the qubit anharmonicities are set to -330 and 3.8 MHz, respectively. The top (bottom) panels show the grayscale plot of first-order (second-order) Floquet collision angles, respectively. The colored lines and their labels represent the corresponding frequency or Floquet collisions. (a) Sweeping the CR drive amplitude $\Omega_c/2\pi$ from -100 to 100 MHz. (b) Sweeping the rotary-tone drive amplitude $\Omega_t/2\pi$ from -5 to 5 MHz. (c) Sweeping the frequency detuning between control and spectator qubits $\Delta_{cs}/2\pi$ from -1 to 1 GHz.

qubits, where $\sigma_{i,j}$ denotes the Pauli operator of the data qubit in the jth row and the ith column. The gauge and stabilizer groups of the heavy-hexagon code are given as follows:

$$\mathcal{G}_{\mathrm{hex}} = \langle Z_{i,j}Z_{i+1,j}, X_{i,j}X_{i,j+1}X_{i+1,j}X_{i+1,j+1},$$
$$X_{1,2m-1}X_{1,2m}, X_{d,2m}X_{d,2m+1} \rangle, \tag{50}$$

$$\mathcal{S}_{\mathrm{hex}} = \langle Z_{i,j}Z_{i,j+1}Z_{i+1,j}Z_{i+1,j+1}, Z_{2m,d}Z_{2m+1,d},$$
$$Z_{2m-1,1}Z_{2m,1}, \prod_i X_{i,j}X_{i,j+1} \rangle, \tag{51}$$

where $m \in [1, 2, \ldots, (d-1)/2]$, and $i + j$ is constrained to be even for the second term in the gauge group and odd for the first term in the stabilizer group. Figure 7(a) shows a geometrical layout of the simultaneous CR drives named $\{P_i\}_{i=0}^6$ in an error syndrome extraction procedure of the heavy-hexagon code. Arrows represent the CR drives in the syndrome extraction, from the control to the target, where those with index i belong to the simultaneous CR drives P_i, and are executed simultaneously.

In principle, each qubit in the heavy-hexagon lattice can have different parameters, which makes the collision anlaysis too high a degree of freedom to discuss. Therefore, we focus on the topological analysis of the Floquet Hamiltonian of the heavy-hexagon code, and discuss

potential Floquet (frequency) collisions in a parameter-independent way. Here, we count up to the second-order potential Floquet (frequency) collisions in the heavy-hexagon code by applying Algorithm 2. A potential kth-order Floquet collision involving the center qubit is defined as a pair of Floquet states satisfying the following conditions:

(1) Pairs that are mapped by translation of the BZ index are treated as identical (Sec. II).
(2) The pair must contain at least one computational state (Sec. IV).
(3) The pair must be coupled via a walk of length k in the Floquet Hamiltonian (Sec. III B).
(4) The walk must be valid and involves the center qubit (Sec. III C).

The corresponding potential kth-order frequency collisions are then defined as the frequency conditions under which bare Floquet quasiexcitation energies of any two of the Floquet states in the valid walk of the kth-order Floquet collision become degenerate.

According to Sec. III C, for the quantitative calculation of the values of the collision angles of the Floquet collisions involving a center qubit, we have to consider the sublattice consisting of qubits within distance $\lfloor 3k/2 \rfloor$.
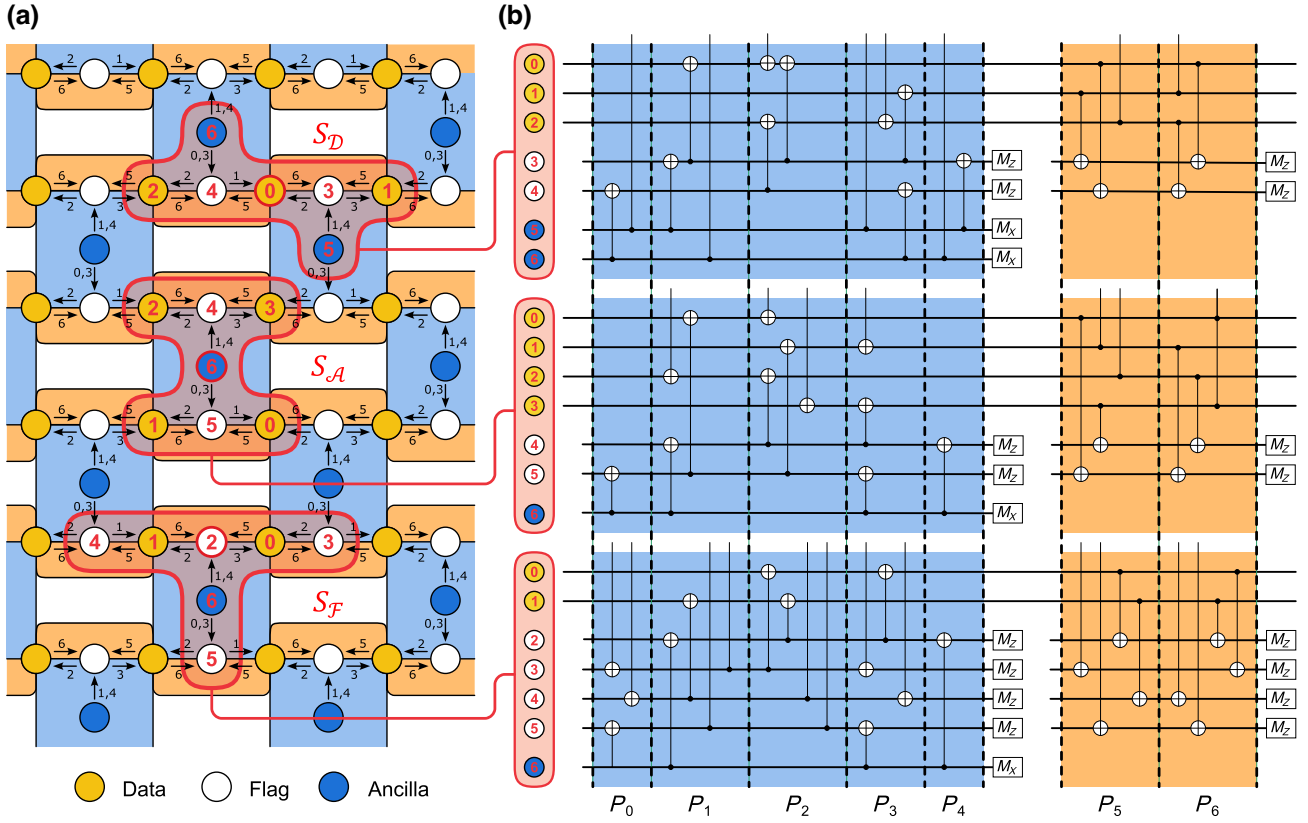
FIG. 7.   Procedures of the error syndrome extraction for the heavy-hexagon code [52], consisting of seven types of simultaneous CR drives labeled $\{P_i\}_{i=0}^6$. Yellow, blue, or white circles correspond to the data, ancilla, and flag qubits, respectively. Blue and orange tiles represent the Z- and X-type parity measurements. Red frames represent sublattices $S_{\mathcal{D},\mathcal{A},\mathcal{F}}$ consisting of qubits only within a distance of 2 from the center data, ancilla, or flag qubit, respectively. The red labels of the qubits represent the qubit correspondence between (a),(b). (a) Geometrical layout of the qubits and simultaneous CR drives on the heavy-hexagonal lattice. Arrows represent CR drives from the control to the target qubit, where the label i belongs to the scheduling P_i. (b) Quantum circuit representations of the syndrome extraction procedures on the sublattices $S_{\mathcal{D},\mathcal{A},\mathcal{F}}$. Each circuit consists of the simultaneous CR drives $\{P_i\}_{i=0}^6$ separated by black dotted lines and the parity measurements. The rectangles labeled with $M_{Z,X}$ represent the projective measurements on the respective axes. If the control or target qubits are outside the sublattices, the other end of the CNOT gate is shown as the open end.

For counting the number of the up to kth-order potential Floquet (frequency) collisions, however, the distance is reduced to k, because we do not need to calculate the energy shifts on the colliding Floquet states, but only search for the valid walks of length k between them. In Fig. 7(a), red frames represent sublattices $S_{\mathcal{D},\mathcal{A},\mathcal{F}}$ consisting of qubits only within a distance of 2 from the center data, ancilla, or flag qubit, respectively. Figure 7(b) shows the quantum circuit representations of the syndrome extraction procedures on the sublattices $S_{\mathcal{D},\mathcal{A},\mathcal{F}}$. If the control or target qubits are outside the sublattices, the other end of the CNOT gate is shown as the open end. As shown in Fig. 7(b), the simultaneous CR drives correspond to mono-to quadmodal Hamiltonian on seven-qubit systems.

Consider the operation basis of simultaneous CR drives. Suppose n simultaneous CR drives, with the ith CR drive between the control qubit c_i and target qubit t_i. In the heavy-hexagon code, the control and target qubits of each CR drive do not overlap with those of other CR drives. All CR drives have different drive frequencies and are assigned different BZ index n_i. Therefore, the operation basis of the simultaneous CR drives is given as the tensor product of the operation basis of the ith CR drive [Eq. (46)]:

$$|\vec{c}, \vec{t}; \vec{\mathbf{n}}\rangle = \bigotimes_i |c_i, t_i; n_i\rangle . \qquad (52)$$

In the heavy-hexagon code, there are also spectator qubits, which should be sufficiently detuned from any CR drives, and hence idle under ideal control. The operation basis with spectator qubits $\vec{s}$ is written as follows:

$$|\vec{c}, \vec{t}, \vec{s}; \vec{\mathbf{n}}\rangle = \left(\bigotimes_i |c_i, t_i; n_i\rangle \right) \otimes \left(\bigotimes_j |s_j\rangle \right), \qquad (53)$$

TABLE IV. Numerical simulations of Algorithm 2 for syndrome extraction procedures on the heavy-hexagon code. The vertical and horizontal axes of the table correspond to the sublattices $S_{\mathcal{D,A,F}}$ and simultaneous CR drives $\{P_i\}_{i=0}^{6}$ subject to Algorithm 2, respectively. In each column, $n_F^{(k)}$ and $n_f^{(k)}$ are the number of kth-order Floquet (frequency) collisions, respectively. A more detailed discussion is provided in Sec. V C.

		P_0	P_1	P_2	P_3	P_4	P_5	P_6
$S_{\mathcal{D}}$	$n_F^{(1)}$	416	416	640	1344	416	640	640
	$n_F^{(2)}$	2432	4224	5312	9728	2432	4992	4992
	$n_f^{(1)}$	6	6	6	6	6	6	6
	$n_f^{(2)}$	77	77	71	94	77	97	97
$S_{\mathcal{A}}$	$n_F^{(1)}$	416	416	192	416	416	640	640
	$n_F^{(2)}$	2432	4224	1920	4224	2432	4992	4992
	$n_f^{(1)}$	6	6	6	6	6	6	6
	$n_f^{(2)}$	77	77	57	77	77	97	97
$S_{\mathcal{F}}$	$n_F^{(1)}$	288	1664	736	512	960	960	960
	$n_F^{(2)}$	1728	10624	4736	4480	4224	7488	7488
	$n_f^{(1)}$	9	9	9	9	9	9	9
	$n_f^{(2)}$	63	110	87	75	95	95	95

where $s_j \in [g, e, f, \ldots]$ represents the jth spectator qubit state. Note that even in the case where multiple CR drives share their control or target qubits [29,95,96], we can define the operation basis as an entangling Floquet state between qubits and analyze Floquet collisions. However, for systems with a nonlocal operation basis, the sublattice extraction procedure in Algorithm 2 requires some adjustments, which is discussed in Appendix D.

Following the procedures of Algorithm 2, we apply Algorithm 1 to simultaneous CR drives $\{P_i\}_{i=0}^{6}$ on the sublattices $S_{\mathcal{D,A,F}}$ as a subroutine of Algorithm 2. The numerical calculation consists of the following procedures. First, an empty graph G_F is created. Based on the given sublattice S_x and the simultaneous CR drives P_y, 2^7-computational states are computed as the operation basis, based on Eq. (53), and added to the graph G_F as nodes. Note that due to the translational symmetry of the Floquet Hamiltonian with respect to the BZ index, the same results are obtained for any choice of the BZ indices of the initial computational states. Since the operation basis is in a tensor product state, even if one of the control and target qubits is outside the sublattice, the operation basis of the other qubit remains intact. The exchange interactions and microwave drives in the sublattices are transformed into perturbations in the Floquet Hamiltonian according to Eq. (3), and regarded as the edges in the graph G_F. We then extract the region, which is reachable by tracing the edges k times from the initial nodes. Finally, in this region, we search for up to second-order potential frequency and Floquet collisions.

Table IV shows the results of the numerical Floquet analysis. The indices $n_F^{(k)}$ and $n_f^{(k)}$ represent the number of

potential kth-order Floquet (frequency) collisions, respectively. An interesting observation is that two symmetric sequences have the same number of Floquet (frequency) collisions. Here, symmetric sequences are those that are equivalent by mirroring while preserving the center qubit. In particular, P_0 and P_4, P_5 and P_6 in $S_{\mathcal{D}}$, and P_0 and P_4, P_1 and P_3, P_5 and P_6 in $S_{\mathcal{A}}$ fall under the symmetric sequences. Moreover, from Table IV and Fig. 7(a), we find that the number of first- and second-order Floquet collisions depends only on the position of the target qubits within the distances 1 and 2 from the center qubit, respectively. As shown in the region within the distance of 2 from the computational Floquet states in Fig. 4, there are no Floquet states accessible only via the microwave drives. Since the number of potential Floquet collisions is only determined by the topological structure of the Floquet energy-level diagram, it can be seen that only the position of the target qubits matters. The microwave drives, however, have a quantitative effect on the collision factors, as found in Tables I and II. Table IV shows also that the number of frequency collisions is much smaller than those of Floquet collisions, suggesting that for a given frequency collision, numerous Floquet collisions occur simultaneously, as in Sec. V B. Table IV shows also that the number of first-order frequency collisions, involving a center qubit, is independent of the sequence and is always 3 times the number of neighboring qubits, since the first-order Floquet collision factor is always nonzero, regardless of the CR drive as found in Tables I and II. Therefore, the center qubit always has one type-1 and two type-3 collisions with the neighboring qubits independently. On the other hand, the number of second-order frequency collisions depends

on the CR drives, since the corresponding Floquet collision factors can be zero depending on the presence or absence of the CR drive based on Tables I and II.

The number of potential Floquet (frequency) collisions for the desired control on a given lattice is a useful quantitative indicator of the difficulty of system-frequency allocation. In principle, we can also calculate the values of the collision angles quantitatively for a given set of system parameters. In reality, system parameters may get finite variation due to fabrication imperfection [49]. Such parameter variation can be also considered by Monte Carlo sampling [97] and our method can provide robust parameter design for the syndrome extraction operation of the heavy-hexagon code. Our current implementation takes about several hours to check up to second-order Floquet collisions involving a particular qubit in the heavy-hexagon code for a given system parameter. However, we expect that methods compatible with high-performance computing, such as tensor networks [98], can drastically reduce the computational time in the future.

VI. SUMMARY AND DISCUSSION

In this paper, we employ Floquet theory to the analysis of frequency collisions. We quantitatively formulate Floquet collisions by collision angles between Floquet states in the operation basis. We show that the collision angles can be calculated with finite computational complexity using a perturbative approach. In the perturbative analysis of Floquet collisions, we introduce a collision order and show the relation between the lower bound on the collision order and the distance in Floquet and real space. Using this relation, we propose an efficient collision analysis method for general and sparse qubit lattices and estimate their computational complexities.

We apply these methods to relevant experimental situations. First, for an ideal two-transmon qubit CR gate and a three-transmon extension, we performed analytical perturbative calculations of the collision bounds, which have been investigated numerically so far [49]. Next, we observed the nature of the Floquet (frequency) collisions through numerical simulations. The simulations show two overlooked collision mechanisms: the type-8 collision and the collision avoided crossing. Type 8 is the collision caused by the *ZZ* interaction between qubits, which implies that unless the *ZZ* interaction is eliminated [31,99], CR gates always have the Floquet collision at the pulse edges, regardless of the control-target detuning. We also show that the rotary tone [51] can modulate the Floquet Hamiltonian and potentially mitigate the type-8 collision. Collision-avoided crossing is the anticrossing effect between the frequency collisions derived from simultaneous Floquet collisions. It suggests that frequency allocation in large-scale quantum processors requires additional attention compared to the conventional frequency allocation in small-scale quantum processors [39,49]. Finally, we analyzed the more complex problem of frequency collisions in heavy-hexagon codes, where we give a quantitative estimation of the difficulty of the system-frequency allocation.

We note that our proposal has a wide range of applications beyond microwave-activated quantum gates between transmon qubits [26–35]. In principle, our proposal is applicable to general quantum operations using periodic drives, including parametric quantum gates [100–103], pulsed qubit reset [104–108], or active qubit-frequency allocation using drive-induced Stark shifts [40,109,110]. Our proposal is also applicable to the quantum processors based on the other solid-state qubits such as fluxonium qubits [111], semiconductor spin qubits [112], trapped ions [113], or N-*V* centers [114]. Our Floquet-based collision analysis provides a way to compare the stability of different quantum controls in various quantum processors on a unified scale.

Our analysis imposed several approximations to the considered system and control. For a more realistic analysis, we have the following prospects. First, we modeled transmon qubits as weakly nonlinear Duffing oscillators, as the leading approximation of the Josephson nonlinearity [89]. In particular, the higher excited levels of transmon are more sensitive to charge dispersion [89,90]. Therefore, collisions that involve such high-energy excited states, e.g., due to high-power off-resonant drive in dispersive protocols [115–121], are very sensitive to charge noise. Transmon qubits also have finite coherence times due to coupling to the environment and noise. Since transitions are generally broadened by the finite coherence time, collision bounds are also expected to be broadened. Some extensions of the Floquet [122] and perturbation theory [123] are applicable to open systems. Taking into account such overlooked features will allow for a more precise characterization of frequency collisions.

Second, we approximated control signals as CW drives, while in practice the control signals have a finite duration pulse envelope. Control signal envelopes lead to a time variation of the effective Hamiltonian [46]. The steep time variation of the Hamiltonian induces nonadiabatic transitions between the instantaneous eigenstates [124,125]. A closed loop in the control parameter space is known to induce a Berry phase to the final state [126]. Similar phenomena is also reported for the Floquet Hamiltonian [127–129]. A Floquet analysis, while incorporating the control signal envelopes [67,129], will provide robust control against frequency collisions.

APPENDIX A: GENERALIZED PERTURBATION THEORY

In this Appendix, we provide the detailed discussion to derive the higher-order effective Hamiltonian using the generalized perturbation theory. As in Sec. III, let H denote the Hamiltonian consisting of the bare term K and perturbation term V, and G the frame operator for diagonalizing the Hamiltonian. Let us assume the polynomial expansions of G and $\mathcal{G}$ with respect to V as follows:

$$G = \sum_{i=1}^{\infty} G_i \quad (G_i \propto V^i), \tag{A1}$$

$$\mathcal{G} = \sum_{i=1}^{\infty} \mathcal{G}_i \quad (\mathcal{G}_i(H) = [G_i]H). \tag{A2}$$

Then, the transformed Hamiltonian will be written as

$$e^{\mathcal{G}}(H) = \left\{ \sum_{i=0}^{\infty} \frac{\left(\sum_{j=1}^{\infty} \mathcal{G}_j \right)^i}{i!} \right\}(H), \tag{A3}$$

and its polynomial expansions with respect to V are written as follows:

$$e^{\mathcal{G}}(H) = \sum_{i=0}^{\infty} W^{(i)} \quad \left(W^{(i)} \propto V^i \right), \tag{A4}$$

where $W^{(i)}$ represents a ith-order energy shift and is written as follows:

$$W^{(i=0)} = K, \tag{A5}$$

$$W^{(i=1)} = \mathcal{G}_1(K) + V, \tag{A6}$$

$$W^{(i\geq 2)} = \sum_{j=1}^{i} \left\{ \frac{1}{j!} \sum_{\substack{\vec{\mathbf{n}} \in \mathbb{N}^j \\ \|\vec{\mathbf{n}}\|_1 = i}} \left(\prod_{n \in \vec{\mathbf{n}}} \mathcal{G}_n \right)(K) \right\}$$
$$+ \sum_{j=1}^{i-1} \left\{ \frac{1}{j!} \sum_{\substack{\vec{\mathbf{n}} \in \mathbb{N}^j \\ \|\vec{\mathbf{n}}\|_1 = i-1}} \left(\prod_{n \in \vec{\mathbf{n}}} \mathcal{G}_n \right)(V) \right\}. \tag{A7}$$

We then enforce Eq. (31) at each order:

$$[W^{(i)}, K] = 0, \tag{A8}$$

from which the frame operators G_i for $i \geq 1$ are derived sequentially as follows:

$$G_i = (\mathcal{D}_K \circ \mathcal{P}_K)\left(W^{(i)} - \mathcal{G}_i(K) \right), \tag{A9}$$

where we use the spectrum decomposition

$$K \equiv \sum_n \kappa_n K_n, \tag{A10}$$

and the following superoperators:

$$\mathcal{D}_K(X) \equiv \sum_{n \neq m} \frac{K_n X K_m}{\kappa_n - \kappa_m}, \tag{A11}$$

$$\mathcal{P}_K(X) \equiv X - \sum_n K_n X K_n. \tag{A12}$$

From Eqs. (A7) and (A9), we note that the term $W^{(i)} - \mathcal{G}_i(K)$ consists of only K, V and $\{G_j\}_{j<i}$.

Suppose the frame operator $G^{(k)}$, truncated up to kth order in perturbation, is as follows:

$$G^{(k)} = \sum_{i=1}^{k} G_i. \tag{A13}$$

The kth-order approximation of the Hamiltonian transformed by $G^{(k-1)}$ is found as

$$H^{(k)} = \sum_{i=0}^{k} W^{(i)} - \mathcal{G}_k(K). \tag{A14}$$

From Eq. (A14), the frame change with operator $G^{(k)}$ can be regarded as a perturbative diagonalization up to the kth order. Finally, we obtained the Hamiltonian $H^{(k)}$ as the kth-order effective Hamiltonian.
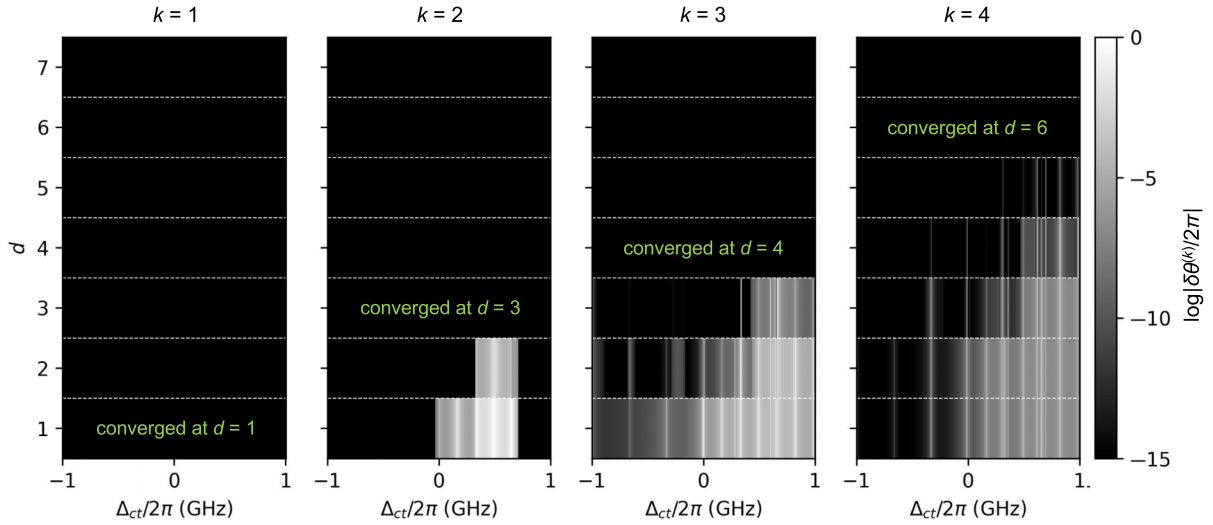
FIG. 8.   Numerical tests of the distance law of the collision order in Sec. III B, for a two-transmon system with a CR drive. Each figure shows the grayscale log plot of the convergence error $\delta\theta^{(k)}$ of the kth-order Floquet collisions from $k = 1$ to 4. In each figure, we perform a 2D sweep of the control-target detuning $\Delta_{ct}/2\pi$ from -1 to 1 GHz and the collision search distance d from 1 to 7. Qubits anharmonicity and qubit-qubit coupling are set to -330 and 3.8 MHz, respectively.

APPENDIX B: PROOF OF EQ. (36)

In this Appendix, we give a proof of Eq. (36). From Eq. (A7), we can represent the kth-order effective Floquet Hamiltonian $H^{(k)}$ as follows:

$$H^{(k)} = \text{Poly}\left(V^k, K^x, \mathcal{D}_K^y, \mathcal{P}_K^y\right), \qquad \text{(B1)}$$

where $x, y \in \mathbb{N}$. Since K and $\mathcal{D}_K$ are diagonal in the operation basis, they do not change the dimension of $\mathcal{S}^{(k)}(|\psi\rangle)$ such that

$$\mathcal{S}^{(k)}(|\psi\rangle) = \text{span}\left(\text{Poly}\left(V^k, \mathcal{P}_K^y\right)|\psi\rangle\right). \qquad \text{(B2)}$$

For a space $\mathcal{S}$ and matrix X, $\mathcal{P}_K$ holds the following property:

$$\text{span}\left(\mathcal{P}_K(X)S\right) \in \text{span}(XS). \qquad \text{(B3)}$$

Therefore, we prove Eq. (36) as follows:

$$\mathcal{S}^{(k)}(|\psi\rangle) \in \text{span}\left(V^k|\psi\rangle\right) \Rightarrow \mathcal{S}^{(k\leq)}(|\psi\rangle) \in \mathbb{K}_k(V, |\psi\rangle). \qquad \text{(B4)}$$

APPENDIX C: NUMERICAL TEST OF THE DISTANCE LAW OF THE COLLISION ORDERS

In Sec. III B, we proved an analytical distance law of the collision order on the Floquet space. In this Appendix, we re-examine the distance law using numerical simulations. Let us assume the CR drive on a two-transmon system, as in Sec. V B. In Sec. V B, we analyzed the kth-order Floquet collision from the Floquet subspace within the search distance $d = \lfloor 3k/2 \rfloor$ from the computational states. In this Appendix, we numerically check the convergence of the collision angles while sweeping the search distance. In the simulation, we define the convergence error $\delta\theta^{(k)}$ as the difference between the kth-order collision angle derived with a sufficiently large search distance ($d = 7$) and with a smaller search distance ($d \leq 6$). Figure 8 shows a grayscale log plot of the convergence error for up to the fourth-order Floquet collisions with 2D sweep of the control-target detuning and the search distance. Figure 8 shows that the convergence error decreases monotonically with increasing the search distance and converges to zero at a particular search distance corresponding to the collision order. From Fig. 8, we can find that the search distance $d = \lfloor 3k/2 \rfloor$ is sufficient to converge $\delta\theta^{(k)} = 0$ for any control-target detuning Δ_{ct} as predicted in Sec. III B.

APPENDIX D: COLLISION ANALYSIS FOR SPARSE QUBIT LATTICE WITH NONLOCAL OPERATION BASIS

In this paper, we have mainly focused on two-qubit gates with a local operation basis, such as the CR gates. As shown in Eq. (46), the operation basis of the CR gate can be written by tensor product states for each qubit. The same applies to other local gates such as CZ and Toffoli gates. On the other hand, the operation basis of the nonlocal gates, such as iSWAP and SWAP gates, form entangling states between qubits. For example, in the case of the cross-cross resonance gate [29], the operation basis in the

---

1: Regard qubit subsets sharing the non-local operation basis as a single node
2: Construct a graph G'_R consisting of such nodes
3: **for** center node from the graph G'_R **do**
4:     Extract a sublattice including only the nodes within distance $\lfloor 3k/2 \rfloor$ from the center node
5:     Construct a subspace Hamiltonian H^{sub} corresponding to the sublattice
6:     **for** qubit from the center node **do**
7:         Verify kth-order Floquet collisions involving the qubit with Algorithm 1
8:     Remove the center node from the graph G'_R

Algorithm 3.   Collision analysis for sparse qubit lattice with nonlocal gates

computational subspace is given as

$$|\psi_0\rangle = \frac{1}{2} \left(-|00\rangle + |01\rangle + |10\rangle + |11\rangle \right), \quad \text{(D1)}$$

$$|\psi_1\rangle = \frac{1}{2} \left(+|00\rangle - |01\rangle + |10\rangle + |11\rangle \right), \quad \text{(D2)}$$

$$|\psi_2\rangle = \frac{1}{2} \left(+|00\rangle + |01\rangle - |10\rangle + |11\rangle \right), \quad \text{(D3)}$$

$$|\psi_3\rangle = \frac{1}{2} \left(+|00\rangle + |01\rangle + |10\rangle - |11\rangle \right), \quad \text{(D4)}$$

where we have omitted the BZ indices for simplicity. In such cases, we should be careful about the sublattice extraction procedure in Algorithm 2, because the qubits sharing the entangling operation basis are indivisible. We summarise our Floquet-based collision analysis for the sparse qubit lattice with nonlocal gates in Algorithm 3. In Algorithm 3, we first map a subset of qubits sharing

the entangling operation basis as a single collective node. Then, we reconstruct the graph G'_R from such nodes, where each collective node couples to all the nodes originally coupled to the qubits in that node. Next, we select the center node of the graph G'_R and extract the sublattice consisting only of nodes within a distance $d = \lfloor 3k/2 \rfloor$. The rest of the procedure is the same as in Algorithm 2. Figure 9 shows an overview of the sublattice extraction in Algorithm 3.

Consider the computational complexity of Algorithm 3. If the entire system is contained in a single many-body nonlocal gate, the computational complexity of Algorithm 3 is equal to Eq. (40). On the other hand, for the case where the system is filled with at most x-body nonlocal gates, the computational complexity $C_3(k, n, d, m, r, x)$ is calculated as follows. From the discussion in Sec. IV, consider a system of n qudits with d levels, m drives, and degree r. The graph G'_R corresponding to the system then consists of n/x nodes and has degree xr. Each nodes can
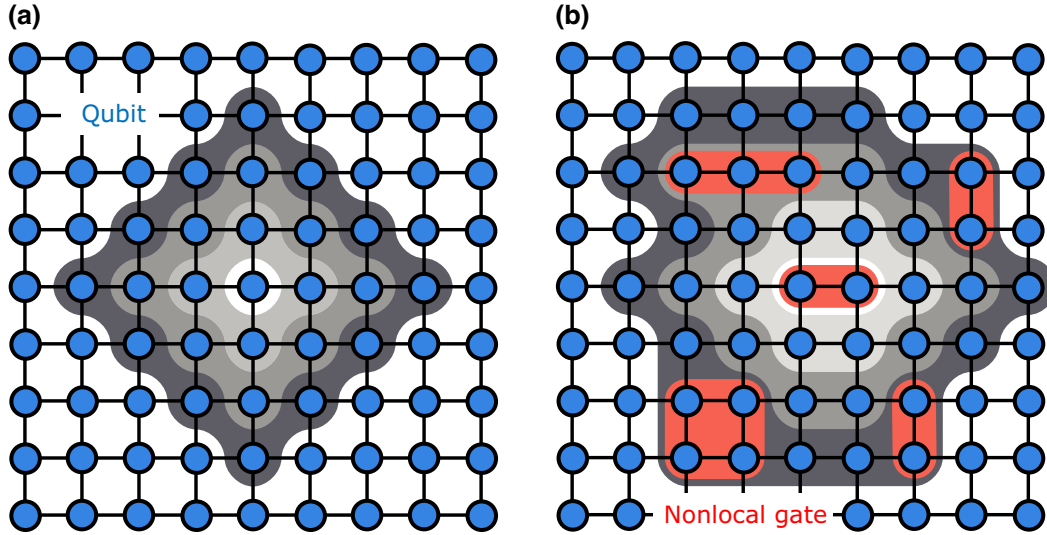

FIG. 9.   Schematic of the distance law of the perturbation order on the sparse qubit lattices without (a) and with (b) the nonlocal gates. The blue circles and black lines represent the qubits and the couplings between them, respectively. (a) The sparse qubit lattice without the nonlocal gates. The gray regions represent the order of the perturbation derived from the center qubit, with darker shades indicating higher order, which depends only on the qubit lattice structure. (b) The sparse qubit lattice with the nonlocal gates. Each subset of qubits grouped in the red region is the target qubit of the each nonlocal gate. The gray regions represent the order of the perturbation derived from the center qubit, with darker shades indicating higher order, which depends both structures of the qubit lattice and non-local gates.

be regarded as d^x-level system with xm drives. Therefore, the computational complexity $C_3(k,n,d,m,r,x)$ is given as follows:

$$C_3(k,n,d,m,r,x) = C_2\left(k, \frac{n}{x}, d^x, xm, xr\right). \qquad \text{(D5)}$$

Equation (D5) increases exponentially with the parameter x and suggests that the presence of nonlocal gates tends to make the collision analysis more difficult.

APPENDIX E: PROPERTIES OF EACH FREQUENCY COLLISION

In this Appendix, we give the properties of each of the frequency collisions introduced in Sec. V B. Types 4 and 8 are omitted here because they were explained in Sec. V B.

Types 1, 3, and 9 correspond to cases where the transition frequencies of the nearest-neighbor qubit pairs are degenerate. In Sec. V B, we dealt with a three-qubit system in which a target and a spectator qubit are coupled to a control qubit, where control and target qubit pairs or control and spectator qubit pairs are corresponding to the nearest-neighbor condition. In type 9, the ef-transition frequencies of both qubits are degenerate.

Types 5 and 6 correspond to the frequency collisions between the next-nearest-neighbor qubit pair. In the system we treated in Sec. V B, the target and spectator qubit pairs correspond to the next-nearest-neighbor condition. In type 5, the ge-transition frequency of one of the qubits is degenerate to that of the other qubit. In type 6, the ge-transition frequency of one of the qubits is degenerate to the ef-transition frequency of the other qubit.

Types 2, 7, 10, 11, and 12 correspond to cases where the cross-resonance transitions are degenerate with microwave-activated transitions. Types 2 and 7 correspond

to cases where $|f,g\rangle$-$|g,e\rangle$ [28] transition between control and target or spectator qubits are degenerate, respectively. Type 10 corresponds to the case where $|h,g\rangle$-$|f,e\rangle$ transition degenerate. Types 11 and 12 correspond to cases where $|h,g\rangle$-$|e,e\rangle$ transition between control and target or spectator qubits are degenerate, respectively. Types 2, 11, 10 also have degenerate two-photon gf, two-photon eh, and fh transitions in the control qubits, respectively.

APPENDIX F: COMPARISON TO THE TIME-DOMAIN SIMULATION

In this Appendix, we compare the predictions of Floquet-based collision analysis, including the collision-avoided crossing, with actual pulse control errors in time-domain simulations. We consider the case where a single CR drive is applied to a three-qubit system, including the spectator qubit introduced in Sec. V B. The CR drive has a raised cosine flattop pulse shape with a maximum intensity of 30 MHz and a full width of 140 ns with a rise time of 20 ns. In the simulation, the propagator driven by the CR drive was calculated while sweeping the detuning between the qubits. To save the simulation time, all qubits were treated up to the third excited level. Figure 10(a) shows a color plot of the collision components, which are defined as the sum of the off-diagonal components in the propagator on the operation basis as

$$p_{\text{out}} = \frac{1}{4} \sum_{s \in [0,1]} \sum_{c \in [0,1]} \left(2 - |\langle sc0| U |sc0\rangle|^2 \right. \qquad \text{(F1)}$$

$$\left. - 2|\langle sc0| U |sc1\rangle|^2 - |\langle sc1| U |sc1\rangle|^2\right), \qquad \text{(F2)}$$

where the $|sct\rangle$ state represents the tensor product state of the s, c, and t states of the spectator, control, and target
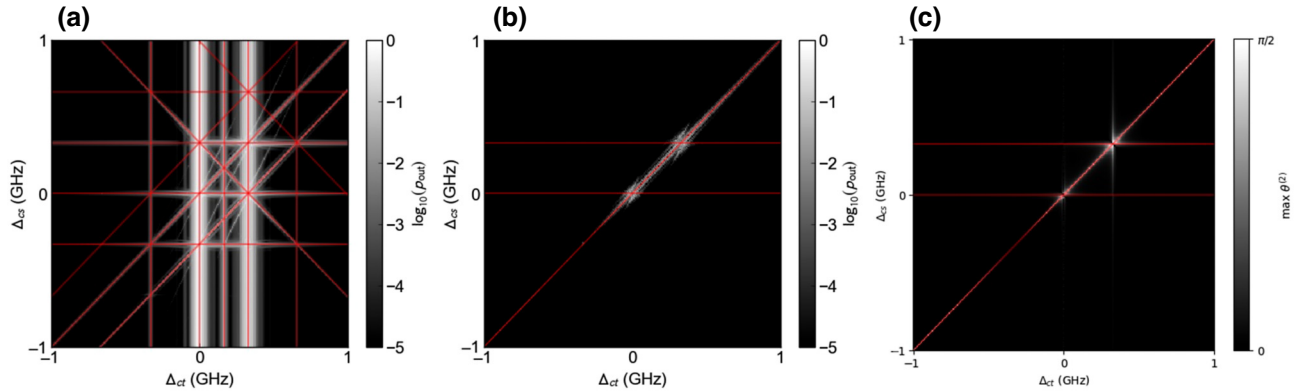

FIG. 10. Numerical simulations of frequency collisions for a CR drive on three transmon system with 2D sweep of system parameters. The sweeping system parameters is the control target $\Delta_{ct}/2\pi$ and control spectator $\Delta_{cs}/2\pi$ detuning from -1 to 1 GHz. Qubit anharmonicities qubit-qubit coupling strength is set to -330 and 3.8 MHz, respectively. The red lines represent the preknown frequency collisions. (a) All collision components in the propagator given by the time-domain simulation. (b) The specific collision components in the propagator given by the time-domain simulation. (c) The specific collision components in the propagator given by the Floquet-based collision analysis.

qubits, respectively. In Fig. 10(a), higher-order frequency collisions also appear as peaks in addition to the up to the second-order frequency collisions predicted in the paper shown by the red line. To confirm the existence of the collision-avoided crossing, we extract the specific transitions $|01+\rangle \leftrightarrow |11+\rangle$ from Fig. 10(a) and plot them in Fig. 10(b). Figure 10(c) shows the same transitions computed by Floquet-based collision analysis. Conventional theory [36,43,45] suggests that this transition occurs only in the type-5 condition, which is indicated by the off-diagonal red line in Fig. 10(b). However, in Fig. 10(b), this transition is confirmed to have a collision avoided crossing at the intersection of type 5 and types 1 and 3. This result is qualitatively consistent with the result of the Floquet-based collision analysis in Fig. 10(c). These results show that the collision-avoided crossings can appear in actual pulse control.

---

[1] Sergey Brayvi, Oliver Dial, Jay M. Gambetta, and Zaira Nazario, The future of quantum computing with superconducting qubits, J. Appl. Phys. **132**, 160902 (2022).

[2] Yasunobu Nakamura, Yu A. Pashkin, and J. S. Tsai, Coherent control of macroscopic quantum states in a single-Cooper-pair box, Nature **398**, 786 (1999).

[3] Andreas Wallraff, David I. Schuster, Alexandre Blais, Luigi Frunzio, R.-S. Huang, Johannes Majer, Sameer Kumar, Steven M. Girvin, and Robert J. Schoelkopf, Strong coupling of a single photon to a superconducting qubit using circuit quantum electrodynamics, Nature **431**, 162 (2004).

[4] J. Majer, J. M. Chow, J. M. Gambetta, Jens Koch, B. R. Johnson, J. A. Schreier, L. Frunzio, D. I. Schuster, A. A. Houck, A. Wallraff, A. Blais, M. H. Devoret, S. M. Girvin, and R. J. Schoelkopf, Coupling superconducting qubits via a cavity bus, Nature **449**, 443 (2007).

[5] B. Foxen, *et al.*, Qubit compatible superconducting interconnects, Quantum Sci. Technol. **3**, 014005 (2017).

[6] Alysson Gold, J. P. Paquette, Anna Stockklauser, Matthew J. Reagor, M. Sohaib Alam, Andrew Bestwick, Nicolas Didier, Ani Nersisyan, Feyza Oruc, Armin Razavi, Ben Scharmann, Eyob A. Sete, Biswajit Sur, Davide Venturelli, Cody James Winkleblack, Filip Wudarski, Mike Harburn, and Chad Rigetti, Entanglement across separate silicon dies in a modular superconducting qubit device, NPJ Quantum Inf. **7**, 142 (2021).

[7] Morten Kjaergaard, Mollie E. Schwartz, Jochen Braumüller, Philip Krantz, Joel I.-J. Wang, Simon Gustavsson, and William D. Oliver, Superconducting qubits: Current state of play, Annu. Rev. Condens. Matter Phys. **11**, 369 (2020).

[8] Paul D. Nation and Matthew Treinish, Suppressing quantum circuit errors due to system variability, ArXiv:2209.15512 (2022).

[9] Antonio D. Córcoles, Easwar Magesan, Srikanth J. Srinivasan, Andrew W. Cross, Matthias Steffen, Jay M. Gambetta, and Jerry M. Chow, Demonstration of a quantum error detection code using a square lattice of four superconducting qubits, Nat. Commun. **6**, 1 (2015). https://www.nature.com/articles/ncomms7979.

[10] Maika Takita, Andrew W. Cross, A. D. Córcoles, Jerry M. Chow, and Jay M. Gambetta, Experimental demonstration of fault-tolerant state preparation with superconducting qubits, Phys. Rev. Lett. **119**, 180501 (2017).

[11] Christian Kraglund Andersen, Ants Remm, Stefania Lazar, Sebastian Krinner, Nathan Lacroix, Graham J. Norris, Mihai Gabureac, Christopher Eichler, and Andreas Wallraff, Repeated quantum error detection in a surface code, Nat. Phys. **16**, 875 (2020). https://www.nature.com/articles/s41567-020-0920-y.

[12] Sebastian Krinner, Nathan Lacroix, Ants Remm, Agustin Di Paolo, Elie Genois, Catherine Leroux, Christoph Hellings, Stefania Lazar, Francois Swiadek, Johannes Herrmann, Graham J. Norris, Christian Kraglund Andersen, Markus Müller, Alexandre Blais, Christopher Eichler, and Andreas Wallraff, Realizing repeated quantum error correction in a distance-three surface code, Nature **605**, 669 (2021).

[13] Zijun Chen, *et al.*, Exponential suppression of bit or phase errors with cyclic error correction, Nature **595**, 383 (2021).

[14] Edward H. Chen, Theodore J. Yoder, Youngseok Kim, Neereja Sundaresan, Srikanth Srinivasan, Muyuan Li, Antonio D. Córcoles, Andrew W. Cross, and Maika Takita, Calibrated decoders for experimental quantum error correction, Phys. Rev. Lett. **128**, 110504 (2022).

[15] J. F. Marques, B. M. Varbanov, M. S. Moreira, H. Ali, N. Muthusubramanian, C. Zachariadis, F. Battistel, M. Beekman, N. Haider, W. Vlothuizen, A. Bruno, B. M. Terhal, and L. DiCarlo, Logical-qubit operations in an error-detecting surface code, Nat. Phys. **18**, 80 (2022).

[16] Youwei Zhao, *et al.*, Realization of an error-correcting surface code with superconducting qubits, Phys. Rev. Lett. **129**, 030501 (2022).

[17] Neereja Sundaresan, Theodore J. Yoder, Youngseok Kim, Muyuan Li, Edward H. Chen, Grace Harper, Ted Thorbeck, Andrew W. Cross, Antonio D. Córcoles, and Maika Takita, Matching and maximum likelihood decoding of a multi-round subsystem quantum error correction experiment, ArXiv:2203.07205 (2022).

[18] M. D. Hutchings, J. B. Hertzberg, Y. Liu, N. T. Bronn, G. A. Keefe, Markus Brink, Jerry M. Chow, and B. L. T. Plourde, Tunable superconducting qubits with flux-independent coherence, Phys. Rev. Appl. **8**, 044003 (2017).

[19] L. DiCarlo, J. M. Chow, J. M. Gambetta, Lev S. Bishop, B. R. Johnson, D. I. Schuster, J. Majer, A. Blais, L. Frunzio, S. M. Girvin, and R. J. Schoelkopf, Demonstration of two-qubit algorithms with a superconducting quantum processor, Nature **460**, 240 (2009).

[20] R. Barends, J. Kelly, A. Megrant, D. Sank, E. Jeffrey, Y. Chen, Y. Yin, B. Chiaro, J. Mutus, C. Neill, P. O'Malley, P. Roushan, J. Wenner, T. C. White, A. N. Cleland, and John M. Martinis, Coherent Josephson qubit suitable for scalable quantum integrated circuits, Phys. Rev. Lett. **111**, 080502 (2013).

[21] David C. McKay, Stefan Filipp, Antonio Mezzacapo, Easwar Magesan, Jerry M. Chow, and Jay M. Gambetta, Universal gate for fixed-frequency qubits via a tunable bus, Phys. Rev. Appl. **6,** 064007 (2016).

[22] S. A. Caldwell, *et al.*, Parametrically activated entangling gates using transmon qubits, Phys. Rev. Appl. **10,** 034050 (2018).

[23] Yuan Xu, Ji Chu, Jiahao Yuan, Jiawei Qiu, Yuxuan Zhou, Libo Zhang, Xinsheng Tan, Yang Yu, Song Liu, Jian Li, Fei Yan, and Dapeng Yu, High-fidelity, high-scalability two-qubit gate scheme for superconducting qubits, Phys. Rev. Lett. **125,** 240503 (2020).

[24] Youngkyu Sung, Leon Ding, Jochen Braumüller, Antti Vepsäläinen, Bharath Kannan, Morten Kjaergaard, Ami Greene, Gabriel O. Samach, Chris McNally, David Kim, Alexander Melville, Bethany M. Niedzielski, Mollie E. Schwartz, Jonilyn L. Yoder, Terry P. Orlando, Simon Gustavsson, and William D. Oliver, Realization of high-fidelity CZ and ZZ-free iSWAP gates with a tunable coupler, Phys. Rev. X **11,** 021058 (2021).

[25] J. Stehlik, D. M. Zajac, D. L. Underwood, T. Phung, J. Blair, S. Carnevale, D. Klaus, G. A. Keefe, A. Carniol, M. Kumph, Matthias Steffen, and O. E. Dial, Tunable coupling architecture for fixed-frequency transmon superconducting qubits, Phys. Rev. Lett. **127,** 080505 (2021).

[26] Jerry M. Chow, Jay M. Gambetta, Andrew W. Cross, Seth T. Merkel, Chad Rigetti, and M. Steffen, Microwave-activated conditional-phase gate for superconducting qubits, New J. Phys. **15,** 115012 (2013).

[27] Jerry M. Chow, Jay M. Gambetta, A. D. Córcoles, Seth T. Merkel, John A. Smolin, Chad Rigetti, S. Poletto, George A. Keefe, Mary B. Rothwell, J. R. Rozen, Mark B. Ketchen, and M. Steffen, Universal quantum gate set approaching fault-tolerant thresholds with superconducting qubits, Phys. Rev. Lett. **109,** 060501 (2012).

[28] S. Krinner, P. Kurpiers, B. Royer, P. Magnard, I. Tsitsilin, J.-C. Besse, A. Remm, A. Blais, and A. Wallraff, Demonstration of an all-microwave controlled-phase gate between far-detuned qubits, Phys. Rev. Appl. **14,** 044039 (2020).

[29] Kentaro Heya and Naoki Kanazawa, Cross-cross resonance gate, PRX Quantum **2,** 040336 (2021).

[30] Bradley K. Mitchell, Ravi K. Naik, Alexis Morvan, Akel Hashim, John Mark Kreikebaum, Brian Marinelli, Wim Lavrijsen, Kasra Nowrouzi, David I. Santiago, and Irfan Siddiqi, Hardware-efficient microwave-activated tunable coupling between superconducting qubits, Phys. Rev. Lett. **127,** 200502 (2021).

[31] K. X. Wei, E. Magesan, I. Lauer, S. Srinivasan, D. F. Bogorin, S. Carnevale, G. A. Keefe, Y. Kim, D. Klaus, W. Landers, N. Sundaresan, C. Wang, E. J. Zhang, M. Steffen, O. E. Dial, D. C. McKay, and A. Kandala, Hamiltonian engineering with multicolor drives for fast entangling gates and quantum crosstalk cancellation, Phys. Rev. Lett. **129,** 060501 (2022).

[32] A. D. K. Finck, S. Carnevale, D. Klaus, C. Scerbo, J. Blair, T. G. McConkey, C. Kurter, A. Carniol, G. Keefe, M. Kumph, and O. E. Dial, Suppressed crosstalk between two-junction superconducting qubits with mode-selective exchange coupling, Phys. Rev. Appl. **16,** 054041 (2021).

[33] Marie Lu, Jean-Loup Ville, Joachim Cohen, Alexandru Petrescu, Sydney Schreppler, Larry Chen, Christian Jünger, Chiara Pelletti, Alexei Marchenkov, Archan Banerjee, William P. Livingston, John Mark Kreikebaum, David I. Santiago, Alexandre Blais, and Irfan Siddiqi, Multipartite entanglement in Rabi-driven superconducting qubits, PRX Quantum **3,** 040322 (2022).

[34] Long B. Nguyen, Yosep Kim, Akel Hashim, Noah Goss, Brian Marinelli, Bibek Bhandari, Debmalya Das, Ravi K. Naik, John Mark Kreikebaum, Andrew N. Jordan, David I. Santiago, and Irfan Siddiqi, Programmable Heisenberg interactions between Floquet qubits, ArXiv:2211.10383 (2022).

[35] Shotaro Shirai, Yuta Okubo, Kohei Matsuura, Alto Osada, Yasunobu Nakamura, and Atsushi Noguchi, All-microwave manipulation of superconducting qubits with a fixed-frequency transmon coupler, ArXiv:2302.06930 (2023).

[36] Moein Malekakhlagh, Easwar Magesan, and David C. McKay, First-principles analysis of cross-resonance gate operation, Phys. Rev. A **102,** 042605 (2020).

[37] M. Brink, J. M. Chow, J. Hertzberg, E. Magesan, and S. Rosenblatt, in *Proceedings of the 2018 IEEE International Electron Devices Meeting (IEDM)* (2018), p. 6.1.1.

[38] Peng Zhao, Kehuan Linghu, Zhiyuan Li, Peng Xu, Ruixia Wang, Guangming Xue, Yirong Jin, and Haifeng Yu, Quantum crosstalk analysis for simultaneous gate operations on superconducting qubits, PRX Quantum **3,** 020301 (2022).

[39] Eric J. Zhang, *et al.*, High-performance superconducting quantum processors via laser annealing of transmon qubits, Sci. Adv. **8,** eabi6690 (2022).

[40] Hyunseong Kim, Christian Jünger, Alexis Morvan, Edward S. Barnard, William P. Livingston, M. Virginia, P. Altoé, Yosep Kim, Chengyu Song, Larry Chen, John Mark Kreikebaum, D. Frank Ogletree, David I. Santiago, and Irfan Siddiqi, Effects of laser-annealing on fixed-frequency superconducting qubits, Appl. Phys. Lett. **121,** 142601 (2022).

[41] Chad Rigetti and Michel Devoret, Fully microwave-tunable universal gates in superconducting qubits with linear couplings and fixed transition frequencies, Phys. Rev. B **81,** 134507 (2010).

[42] Sarah Sheldon, Easwar Magesan, Jerry M. Chow, and Jay M. Gambetta, Procedure for systematically tuning up cross-talk in the cross-resonance gate, Phys. Rev. A **93,** 060302(R) (2016).

[43] Easwar Magesan and Jay M. Gambetta, Effective Hamiltonian models of the cross-resonance gate, Phys. Rev. A **101,** 052308 (2020).

[44] J. R. Schrieffer and P. A. Wolff, Relation between the Anderson and Kondo hamiltonians, Phys. Rev. **149,** 491 (1966).

[45] Vinay Tripathi, Mostafa Khezri, and Alexander N. Korotkov, Operation and intrinsic error budget of a two-qubit cross-resonance gate, Phys. Rev. A **100,** 012301 (2019).

[46] Moein Malekakhlagh and Easwar Magesan, Mitigating off-resonant error in the cross-resonance gate, Phys. Rev. A **105,** 012602 (2022).

[47] K. X. Wei, E. Pritchett, D. M. Zajac, D. C. Mackay, and S. Merkel, Characterizing non-Markovian off-resonant excitation errors, ArXiv:2302.10881 (2023).

[48] Gaston Floquet, Sur les équations différentielles linéaires à coefficients périodiques, Ann. Sci. de l'Ecole Norm. Superieure **12**, 47 (1883).

[49] Jared B. Hertzberg, Eric J. Zhang, Sami Rosenblatt, Easwar Magesan, John A. Smolin, Jeng-Bang Yau, Vivekananda P. Adiga, Martin Sandberg, Markus Brink, Jerry M. Chow, and Jason S. Orcutt, Laser-annealing Josephson junctions for yielding scaled-up superconducting quantum processors, NPJ Quantum Inf. **7**, 129 (2021).

[50] Hans Primas, Generalized perturbation theory in operator form, Rev. Mod. Phys. **35**, 710 (1963).

[51] Neereja Sundaresan, Isaac Lauer, Emily Pritchett, Easwar Magesan, Petar Jurcevic, and Jay M. Gambetta, Reducing unitary and spectator errors in cross resonance with optimized rotary echoes, PRX Quantum **1**, 020318 (2020).

[52] Christopher Chamberland, Guanyu Zhu, Theodore J. Yoder, Jared B. Hertzberg, and Andrew W. Cross, Topological and subsystem codes on low-degree graphs with flag qubits, Phys. Rev. X **10**, 011022 (2020).

[53] John Dugundji and John H. Wendell, Some analysis methods for rotating systems with periodic coefficients, AIAA J. **21**, 890 (1983).

[54] David A. Peters, Fast Floquet theory and trim for multi-bladed rotorcraft, J. Am. Helicopter Soc. **39**, 82 (1994).

[55] Richard P. Boland, Tobias Galla, and Alan J. McKane, Limit cycles, complex Floquet multipliers, and intrinsic noise, Phys. Rev. E **79**, 051131 (2009).

[56] Takashi Oka and Sota Kitamura, Floquet engineering of quantum materials, Annu. Rev. Condens. Matter Phys. **10**, 387 (2019).

[57] Umberto De Giovannini and Hannes Hübener, Floquet analysis of excitations in materials, J. Phys. Chem. Mater. **3**, 012001 (2019).

[58] Jon H. Shirley, Solution of the Schrödinger equation with a Hamiltonian periodic in time, Phys. Rev. **138**, B979 (1965).

[59] T. O. Levante, M. Baldus, B. H. Meier, and R. R. Ernst, Formalized quantum mechanical Floquet theory and its application to sample spinning in nuclear magnetic resonance, Mol. Phys. **86**, 1195 (1995).

[60] Dominic V. Else, Bela Bauer, and Chetan Nayak, Floquet time crystals, Phys. Rev. Lett. **117**, 090402 (2016).

[61] Frank Arute, *et al.*, Observation of separated dynamics of charge and spin in the Fermi-Hubbard model, ArXiv:2010.07965 (2020).

[62] Anthony Gandon, Camille Le Calonnec, Ross Shillito, Alexandru Petrescu, and Alexandre Blais, Engineering, control, and longitudinal readout of Floquet qubits, Phys. Rev. Appl. **17**, 064006 (2022).

[63] Pranav S. Mundada, András Gyenis, Ziwen Huang, Jens Koch, and Andrew A. Houck, Floquet-engineered enhancement of coherence times in a driven fluxonium qubit, Phys. Rev. Appl. **14**, 054033 (2020).

[64] Ziwen Huang, Pranav S. Mundada, András Gyenis, David I. Schuster, Andrew A. Houck, and Jens Koch, Engineering dynamical sweet spots to protect qubits from $1/f$ noise, Phys. Rev. Appl. **15**, 034065 (2021).

[65] Joseph A. Valery, Shoumik Chowdhury, Glenn Jones, and Nicolas Didier, Dynamical sweet spot engineering via two-tone flux modulation of superconducting qubits, PRX Quantum **3**, 020337 (2022).

[66] Kaidong Peng, Mahdi Naghiloo, Jennifer Wang, Gregory D. Cunningham, Yufeng Ye, and Kevin P. O'Brien, Floquet-mode traveling-wave parametric amplifiers, PRX Quantum **3**, 020306 (2022).

[67] Agustin Di Paolo, Catherine Leroux, Thomas M. Hazard, Kyle Serniak, Simon Gustavsson, Alexandre Blais, and William D. Oliver, Extensible circuit-QED architecture via amplitude- and frequency-variable microwaves, ArXiv:2204.08098 (2022).

[68] Atsushi Noguchi, Alto Osada, Shumpei Masuda, Shingo Kono, Kentaro Heya, S. P. Wolski, Hiroki Takahashi, Takanori Sugiyama, Dany Lachance-Quirion, and Yasunobu Nakamura, Fast parametric two-qubit gates with suppressed residual interaction using the second-order nonlinearity of a cubic transmon, Phys. Rev. A **102**, 062408 (2020).

[69] Hideo Sambe, Steady states and quasienergies of a quantum-mechanical system in an oscillating field, Phys. Rev. A **7**, 2203 (1973).

[70] Jay Gambetta, Alexandre Blais, D. I. Schuster, A. Wallraff, L. Frunzio, J. Majer, M. H. Devoret, S. M. Girvin, and R. J. Schoelkopf, Qubit-photon interactions in a cavity: measurement-induced dephasing and number splitting, Phys. Rev. A **74**, 042318 (2006).

[71] D. I. Schuster, A. A. Houck, J. A. Schreier, A. Wallraff, J. M. Gambetta, A. Blais, L. Frunzio, J. Majer, B. Johnson, M. H. Devoret, S. M. Girvin, and R. J. Schoelkopf, Resolving photon number states in a superconducting circuit, Nature **445**, 515 (2007).

[72] Michael A. Nielsen, A simple formula for the average gate fidelity of a quantum dynamical operation, Phys. Lett. A **303**, 249 (2002).

[73] S. Geršgorin (S. Gerschgorin), "Über die Abgrenzung der Eigenwerte einer Matrix", Bulletin de l'Académie des Sciences de l'URSS. Classe des sciences mathématiques et na (1931), no. 6, p. 749, https://www.mathnet.ru/php/archive.phtml?wshow=paper&jrnid=im&paperid=5235&option_lang=eng.

[74] John William Strutt Baron Rayleigh, *The Theory of Sound* (Macmillan & Company, New York, 1896), Vol. 2. https://www.cambridge.org/core/books/theory-of-sound/63A09A27C9F93C4ECD8C195544C14D57.

[75] F. J. Dyson, The radiation theories of Tomonaga, Schwinger, and Feynman, Phys. Rev. **75**, 486 (1949).

[76] Wilhelm Magnus, On the exponential solution of differential equations for a linear operator, Commun. Pure Appl. Anal. **7**, 649 (1954).

[77] U. Haeberlen and J. S. Waugh, Coherent averaging effects in magnetic resonance, Phys. Rev. **175**, 453 (1968).

[78] Carl M. Bender and Luís M. A. Bettencourt, Multiple-scale analysis of the quantum anharmonic oscillator, Phys. Rev. Lett. **77**, 4114 (1996).

[79] S. Guérin, R. G. Unanyan, L. P. Yatsenko, and H. R. Jauslin, Floquet perturbative analysis for stirap beyond the rotating wave approximation, Opt. Express **4**, 84 (1999).

[80] M. Rodriguez-Vega, Meghan Lentz, and Babak Seradjeh, Floquet perturbation theory: Formalism and application to low-frequency limit, New J. Phys. **20**, 093022 (2018).

[81] Roopayan Ghosh, Bhaskar Mukherjee, and K. Sengupta, Floquet perturbation theory for periodically driven weakly interacting fermions, Phys. Rev. B **102**, 235114 (2020).

[82] Magnus R. Hestenes and Eduard Stiefel, Methods of conjugate gradients for solving, J. Res. Natl. Bur. Stand. **49**, 409 (1952).

[83] Sergey Bravyi, David P. DiVincenzo, and Daniel Loss, Schrieffer–Wolff transformation for quantum many-body systems, Ann. Phys. **326**, 2793 (2011).

[84] Pierre-Louis Giscard and Christian Bonhomme, Dynamics of quantum systems driven by time-varying Hamiltonians: Solution for the Bloch-Siegert Hamiltonian and applications to NMR, Phys. Rev. Res. **2**, 023081 (2020).

[85] Daniel Gottesman, *Stabilizer Codes and Quantum Error Correction* (California Institute of Technology, Pasadena, 1997). https://thesis.library.caltech.edu/2900/2/THESIS.pdf.

[86] Sergey B. Bravyi and A. Yu Kitaev, Quantum codes on a lattice with boundary, ArXiv:quant-ph/9811052 (1998).

[87] Austin G. Fowler, Matteo Mariantoni, John M. Martinis, and Andrew N. Cleland, Surface codes: Towards practical large-scale quantum computation, Phys. Rev. A **86**, 032324 (2012).

[88] H. Bombin and M. A. Martin-Delgado, Topological quantum distillation, Phys. Rev. Lett. **97**, 180501 (2006).

[89] Jens Koch, Terri M. Yu, Jay Gambetta, A. A. Houck, D. I. Schuster, J. Majer, Alexandre Blais, M. H. Devoret, S. M. Girvin, and R. J. Schoelkopf, Charge-insensitive qubit design derived from the Cooper pair box, Phys. Rev. A **76**, 042319 (2007).

[90] J. A. Schreier, A. A. Houck, Jens Koch, D. I. Schuster, B. R. Johnson, J. M. Chow, J. M. Gambetta, J. Majer, L. Frunzio, M. H. Devoret, S. M. Girvin, and R. J. Schoelkopf, Suppressing charge noise decoherence in superconducting charge qubits, Phys. Rev. B **77**, 180502(R) (2008).

[91] Petar Jurcevic, *et al.*, Demonstration of quantum volume 64 on a superconducting quantum computing system, Quantum Sci. Technol. **6**, 025020 (2021).

[92] Dave Bacon, Operator quantum error-correcting subsystems for self-correcting quantum memories, Phys. Rev. A **73**, 012340 (2006).

[93] Panos Aliferis and Andrew W. Cross, Subsystem fault tolerance with the Bacon-Shor code, Phys. Rev. Lett. **98**, 220502 (2007).

[94] David Poulin, Stabilizer formalism for operator quantum error correction, Phys. Rev. Lett. **95**, 230504 (2005).

[95] Kentaro Heya, Yasunari Suzuki, Yasunobu Nakamura, and Keisuke Fujii, Variational quantum gate optimization, ArXiv:1810.12745 (2018).

[96] Yosep Kim, Alexis Morvan, Long B. Nguyen, Ravi K. Naik, Christian Jünger, Larry Chen, John Mark Kreikebaum, David I. Santiago, and Irfan Siddiqi, High-fidelity three-qubit iToffoli gate for fixed-frequency superconducting qubits, Nat. Phys. **18**, 783 (2022).

[97] David John Cameron Mackay, in *Learning in graphical models* (Springer, New York, 1998), p. 175.

[98] Román Orús, A practical introduction to tensor networks: Matrix product states and projected entangled pair states, Ann. Phys. **349**, 117 (2014). https://www.sciencedirect.com/science/article/pii/S0003491614001596.

[99] A. Kandala, K. X. Wei, S. Srinivasan, E. Magesan, S. Carnevale, G. A. Keefe, D. Klaus, O. Dial, and D. C. McKay, Demonstration of a high-fidelity CNOT gate for fixed-frequency transmons with engineered *ZZ* suppression, Phys. Rev. Lett. **127**, 130501 (2021).

[100] Matthew Reagor, *et al.*, Demonstration of universal parametric entangling gates on a multi-qubit lattice, Sci. Adv. **4**, eaao3603 (2018).

[101] Sabrina S. Hong, Alexander T. Papageorge, Prasaht Sivarajah, Genya Crossman, Nicolas Didier, Anthony M. Polloreno, Eyob A. Sete, Stefan W. Turkowski, Marcus P. da Silva, and Blake R. Johnson, Demonstration of a parametrically activated entangling gate protected from flux noise, Phys. Rev. A **101**, 012302 (2020).

[102] Eyob A. Sete, Nicolas Didier, Angela Q. Chen, Shobhan Kulshreshtha, Riccardo Manenti, and Stefano Poletto, Parametric-resonance entangling gates with a tunable coupler, Phys. Rev. Appl. **16**, 024050 (2021).

[103] Kentaro Kubo and Hayato Goto, Fast parametric two-qubit gate for highly detuned fixed-frequency superconducting qubits using a double-transmon coupler, Appl. Phys. Lett. **122**, 064001 (2023).

[104] K. W. Murch, U. Vool, D. Zhou, S. J. Weber, S. M. Girvin, and I. Siddiqi, Cavity-assisted quantum bath engineering, Phys. Rev. Lett. **109**, 183602 (2012).

[105] K. Geerlings, Z. Leghtas, I. M. Pop, S. Shankar, L. Frunzio, R. J. Schoelkopf, M. Mirrahimi, and M. H. Devoret, Demonstrating a driven reset protocol for a superconducting qubit, Phys. Rev. Lett. **110**, 120501 (2013).

[106] D. J. Egger, M. Werninghaus, M. Ganzhorn, G. Salis, A. Fuhrer, P. Müller, and S. Filipp, Pulsed reset protocol for fixed-frequency superconducting qubits, Phys. Rev. Appl. **10**, 044030 (2018).

[107] P. Magnard, P. Kurpiers, B. Royer, T. Walter, J.-C. Besse, S. Gasparinetti, M. Pechal, J. Heinsoo, S. Storz, A. Blais, and A. Wallraff, Fast and unconditional all-microwave reset of a superconducting qubit, Phys. Rev. Lett. **121**, 060502 (2018).

[108] Yu Zhou, Zhenxing Zhang, Zelong Yin, Sainan Huai, Xiu Gu, Xiong Xu, Jonathan Allcock, Fuming Liu, Guanglei Xi, Qiaonian Yu, Hualiang Zhang, Mengyu Zhang, Hekang Li, Xiaohui Song, Zhan Wang, Dongning Zheng, Shuoming An, Yarui Zheng, and Shengyu Zhang, Rapid and unconditional parametric reset protocol for tunable superconducting qubits, Nat. Commun. **12**, 5924 (2021).

[109] Malcolm Carroll, Sami Rosenblatt, Petar Jurcevic, Isaac Lauer, and Abhinav Kandala, Dynamics of superconducting qubit relaxation times, NPJ Quantum Inf. **8**, 132 (2022).

[110] Alexis Morvan, Larry Chen, Jeffrey M. Larson, David I. Santiago, and Irfan Siddiqi, Optimizing frequency

allocation for fixed-frequency superconducting quantum processors, Phys. Rev. Res. **4,** 023079 (2022).

[111] Vladimir E. Manucharyan, Jens Koch, Leonid I. Glazman, and Michel H. Devoret, Fluxonium: Single cooper-pair circuit free of charge offsets, Science **326,** 113 (2009).

[112] Guido Burkard, Thaddeus D. Ladd, Andrew Pan, John M. Nichol, and Jason R. Petta, Semiconductor spin qubits, Rev. Mod. Phys. **95,** 025003 (2023).

[113] Colin D. Bruzewicz, John Chiaverini, Robert McConnell, and Jeremy M. Sage, Trapped-ion quantum computing: Progress and challenges, Appl. Phys. Rev. **6,** 021314 (2019).

[114] Sébastien Pezzagna and Jan Meijer, Quantum computer based on color centers in diamond, Appl. Phys. Rev. **8,** 011308 (2021).

[115] Daniel Sank, *et al.*, Measurement-induced state transitions in a superconducting qubit: Beyond the rotating wave approximation, Phys. Rev. Lett. **117,** 190503 (2016).

[116] Lucas Verney, Raphaël Lescanne, Michel H. Devoret, Zaki Leghtas, and Mazyar Mirrahimi, Structural instability of driven Josephson circuits prevented by an inductive shunt, Phys. Rev. Appl. **11,** 024003 (2019).

[117] Raphaël Lescanne, Lucas Verney, Quentin Ficheux, Michel H. Devoret, Benjamin Huard, Mazyar Mirrahimi, and Zaki Leghtas, Escape of a driven quantum Josephson circuit into unconfined states, Phys. Rev. Appl. **11,** 014030 (2019).

[118] Ross Shillito, Alexandru Petrescu, Joachim Cohen, Jackson Beall, Markus Hauru, Martin Ganahl, Adam G. M. Lewis, Guifre Vidal, and Alexandre Blais, Dynamics of transmon ionization, Phys. Rev. Appl. **18,** 034031 (2022).

[119] Moein Malekakhlagh, William Shanks, and Hanhee Paik, Optimization of the resonator-induced phase gate for superconducting qubits, Phys. Rev. A **105,** 022607 (2022).

[120] Joachim Cohen, Alexandru Petrescu, Ross Shillito, and Alexandre Blais, Reminiscence of classical chaos in driven transmons, ArXiv:2207.09361 (2022).

[121] Mostafa Khezri, *et al.*, Measurement-induced state transitions in a superconducting qubit: Within the rotating wave approximation, ArXiv:2212.05097 (2022).

[122] S. A. Sato, U. De Giovannini, S Aeschlimann, I. Gierz, H. Hübener, and A. Rubio, Floquet states in dissipative open quantum systems, J. Phys. B **53,** 225601 (2020).

[123] Moein Malekakhlagh, Easwar Magesan, and Luke C. G. Govia, Time-dependent Schrieffer-Wolff-Lindblad perturbation theory: Measurement-induced dephasing and second-order Stark shift in dispersive readout, Phys. Rev. A **106,** 052601 (2022).

[124] Max Born and Vladimir Fock, Beweis des adiabatensatzes, Z. Phys. **51,** 165 (1928).

[125] Tosio Kato, On the adiabatic theorem of quantum mechanics, J. Phys. Soc. Jpn. **5,** 435 (1950).

[126] Michael Victor Berry, Quantal phase factors accompanying adiabatic changes, Proc. R. Soc. Lond. A: Math. Phys. Sci. **392,** 45 (1984).

[127] Daniel W. Hone, Roland Ketzmerick, and Walter Kohn, Time-dependent Floquet theory and absence of an adiabatic limit, Phys. Rev. A **56,** 4045 (1997).

[128] Kento Uchida, Satoshi Kusaba, Kohei Nagai, Tatsuhiko N. Ikeda, and Koichiro Tanaka, Diabatic and adiabatic transitions between Floquet states imprinted in coherent exciton emission in monolayer WSe$_2$, Sci. Adv. **8,** eabq7281 (2022).

[129] Phillip Weinberg, Marin Bukov, Luca D'Alessio, Anatoli Polkovnikov, Szabolcs Vajna, and Michael Kolodrubetz, Adiabatic perturbation theory and geometry of periodically-driven systems, Phys. Rep. **688,** 1 (2017).